CellPress

Cell Metabolism
Article

A High-Fat Diet and NAD$^+$ Activate Sirt1 to Rescue Premature Aging in Cockayne Syndrome

Morten Scheibye-Knudsen,[1] Sarah J. Mitchell,[2,5] Evandro F. Fang,[1] Teruaki Iyama,[1] Theresa Ward,[2] James Wang,[1] Christopher A. Dunn,[1] Nagendra Singh,[3] Sebastian Veith,[6] Md Mahdi Hasan-Olive,[4] Aswin Mangerich,[6] Mark A. Wilson,[4] Mark P. Mattson,[4] Linda H. Bergersen,[7,9] Victoria C. Cogger,[5,8] Alessandra Warren,[8] David G. Le Couteur,[5,8] Ruin Moaddel,[3] David M. Wilson III,[1] Deborah L. Croteau,[1] Rafael de Cabo,[2,*] and Vilhelm A. Bohr[1,9,*]

[1]Laboratory of Molecular Gerontology
[2]Translational Gerontology Branch
[3]Laboratory of Clinical Investigation
[4]Laboratory of Neurosciences
National Institute on Aging, National Institutes of Health, Baltimore, MD 21224, USA
[5]Sydney Medical School, University of Sydney, Sydney, NSW 2006, Australia
[6]Molecular Toxicology Group, Department of Biology, University of Konstanz, D-78457 Konstanz, Germany
[7]The Brain and Muscle Energy Group - Synaptic Neurochemistry Laboratory, Department of Anatomy, Institute of Basic Medical Sciences, University of Oslo, 0317 Oslo, Norway
[8]Centre for Education and Research on Ageing and ANZAC Research Institute, Concord Hospital and University of Sydney, Sydney, NSW 2139, Australia
[9]Danish Center for Healthy Aging, ICMM, University of Copenhagen, Copenhagen, Denmark
*Correspondence: decabora@grc.nia.nih.gov (R.d.C.), vbohr@nih.gov (V.A.B.)
http://dx.doi.org/10.1016/j.cmet.2014.10.005

SUMMARY

Cockayne syndrome (CS) is an accelerated aging disorder characterized by progressive neurodegeneration caused by mutations in genes encoding the DNA repair proteins CS group A or B (CSA or CSB). Since dietary interventions can alter neurodegenerative processes, Csb$^{m/m}$ mice were given a high-fat, caloric-restricted, or resveratrol-supplemented diet. High-fat feeding rescued the metabolic, transcriptomic, and behavioral phenotypes of Csb$^{m/m}$ mice. Furthermore, premature aging in CS mice, nematodes, and human cells results from aberrant PARP activation due to deficient DNA repair leading to decreased SIRT1 activity and mitochondrial dysfunction. Notably, β-hydroxybutyrate levels are increased by the high-fat diet, and β-hydroxybutyrate, PARP inhibition, or NAD$^+$ supplementation can activate SIRT1 and rescue CS-associated phenotypes. Mechanistically, CSB can displace activated PARP1 from damaged DNA to limit its activity. This study connects two emerging longevity metabolites, β-hydroxybutyrate and NAD$^+$, through the deacetylase SIRT1 and suggests possible interventions for CS.

INTRODUCTION

Cockayne syndrome (CS) is a progressive neurodegenerative accelerated aging disorder caused by mutations in the CSA or CSB genes, which encode proteins that are involved in DNA repair and transcriptional regulation. Interestingly, Csb$^{m/m}$ mice and CSB-deficient cells have mitochondrial alterations, and CS patients share the same neurodegenerative traits that are seen in many mitochondrial disorders (Scheibye-Knudsen et al., 2013b). Mice are often used for longevity studies; however, models of age-related neuropathologies such as Alzheimer's disease and Parkinson's disease may not reflect normal human brain aging (Jucker, 2010). Csb$^{m/m}$ mice display many features of mild human CS such as smaller brain weight, inner ear pathology, neuroinflammation, and weight loss (Scheibye-Knudsen et al., 2012). The Csb$^{m/m}$ mouse may therefore be a good model for the study of neuronal aging, and interventions that attenuate the CS phenotype may also counteract brain aging in humans.

Poly-ADP-ribose polymerase 1 (PARP1) catalyzes the conversion of NAD$^+$ molecules to poly-ADP-ribose (PAR) and nicotinamide upon binding to DNA damage. PAR is conjugated to histones and other proteins in the vicinity of the DNA lesion and is believed to participate in the modulation of the DNA repair response. Recent progress has shown that PARP1 activation increases with age, perhaps reflecting an age-related increase in DNA damage (Mouchiroud et al., 2013). Although PARP1 is a critical DNA repair enzyme, persistent activation may be harmful for the organism. Indeed, pharmacological inhibition of PARP or supplementation with NAD$^+$ precursors can extend the lifespan of worms, return tissue functionality to a more youthful state in mice, and rescue mitochondrial dysfunction in some DNA repair disorders (Gomes et al., 2013; Fang et al., 2014; Mouchiroud et al., 2013). Interestingly, the NAD$^+$-dependent deacetylase SIRT1 is required for these effects (Gomes et al., 2013; Mouchiroud et al., 2013).

Since different diets can modulate neurodegenerative phenotypes, we investigated the effect of a high-fat diet (HFD), caloric restriction (CR), and resveratrol supplementation on the phenotype of wild-type (WT) and Csb$^{m/m}$ mice. Remarkably, the HFD rescued the metabolic and cerebellar phenotype of the Csb$^{m/m}$ mice. SIRT1 was attenuated in Csb$^{m/m}$ mice, worms, and patient cells due to PARP1 activation and NAD$^+$ depletion.

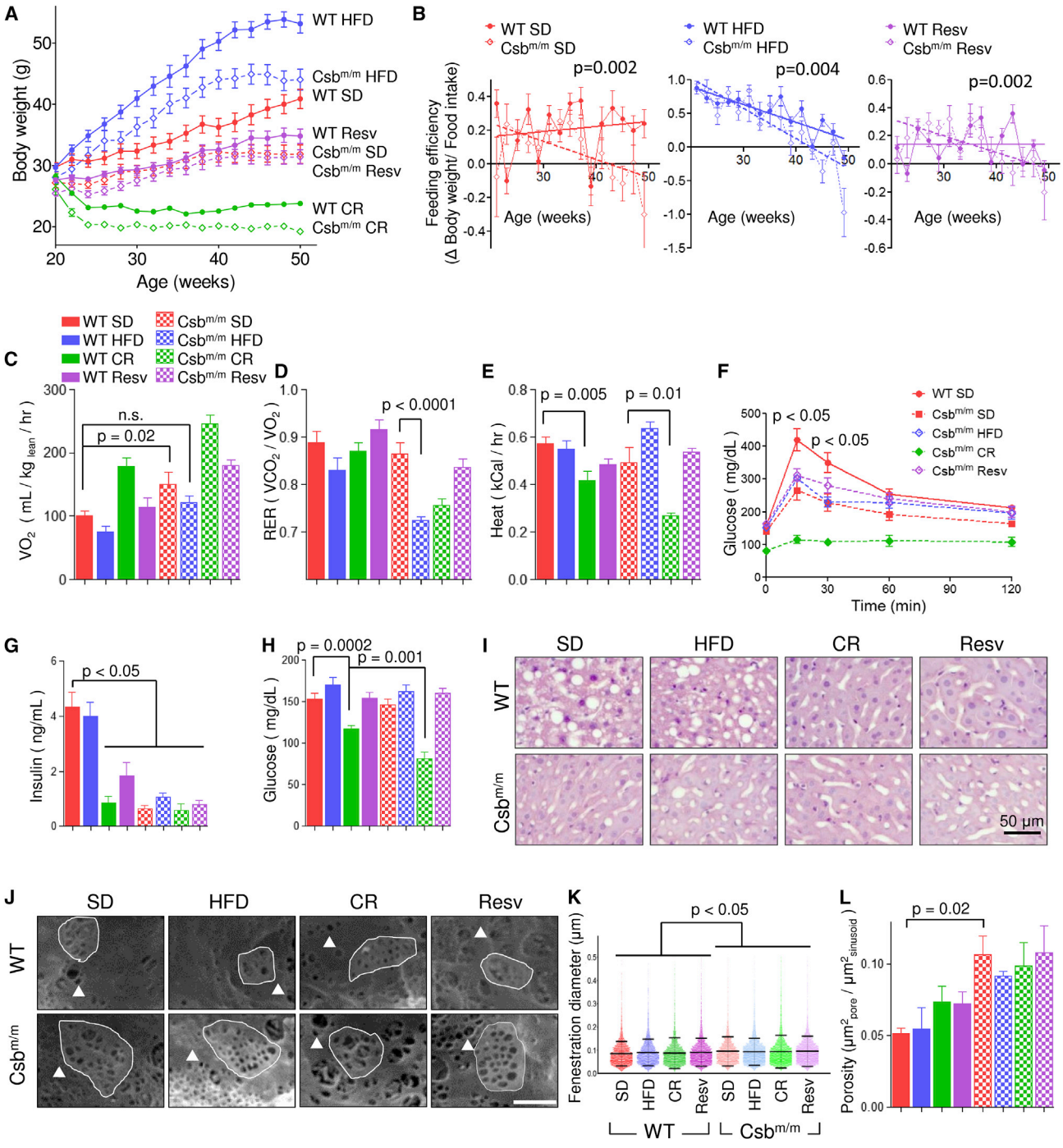

Figure 1. A HFD Rescues the Metabolic Phenotype of Csb$^{m/m}$ Mice

(A) Body weights of WT and Csb$^{m/m}$ mice on various diets; SD: Standard diet; HFD: High fat diet; Resv: resveratrol-supplemented standard diet; CR: Caloric restricted (n = 12–14, mean ± SEM).

(B) Feeding efficiency shown by weight gain per food intake (n = 12–14, mean ± SEM).

(C) Whole-body oxygen consumption over 72 hr (n = 12–14, mean ± SEM).

(D) Respiratory exchange rates (n = 12–14, mean ± SEM).

(E) Heat production (n = 12–14, mean ± SEM).

(F) OGTTs performed after 3 hr fasting (n = 5–9, mean ± SEM).

(G) Insulin levels after 3 hr fasting (n = 7–11, mean ± SEM).

(H) Glucose levels after 3 hr fast (n = 5–9, mean ± SEM).

(I) Representative images of liver histology stained with hematoxylin and eosin.

(legend continued on next page)

β-hydroxybutyrate (β-OHB) levels were increased in the HFD-treated mice, and this ketone body increased SIRT1 expression and activity in CSB-deficient cells. Interestingly, PARP1 inhibition and β-OHB rescued the shortened lifespan of CSB-deficient nematodes. PARP inhibition or supplementation with an NAD^+ precursor rescued metabolic, mitochondrial, and transcriptional alterations in $Csb^{m/m}$ mice. At the molecular level, CSB is able to displace activated PARP1 from damaged DNA, thereby shutting downs its PARylating activity and restoring NAD^+ levels. Considering that CS is an accelerated aging disorder with features similar to late-stage human aging, a ketogenic diet might prove neuroprotective in older individuals, as previously suggested (Maalouf et al., 2009). In addition, since no treatment is currently available for CS patients, NAD^+ augmentation or a ketogenic diet could be adapted for this devastating disease.

RESULTS

A HFD Normalizes the Metabolism of $Csb^{m/m}$ Mice

To test the hypothesis that dietary intervention may ameliorate the metabolic defects exhibited by CS mammalian models, 4-month-old male WT and $Csb^{m/m}$ mice were randomized to 8 months of a standard diet (SD), a HFD (61% kcal from fat and 16% from carbohydrates), a 40% CR SD, and a SD supplemented with 100 mg/kg resveratrol. During the treatment, we monitored bodyweight, food intake, and body temperature to define the consequences of the various dietary interventions (Figure 1A; Figures 1A–S1G available online). Interestingly, $Csb^{m/m}$ mice gained significantly less body weight than WT mice on all diets, with the exception of mice fed resveratrol. Indeed, $Csb^{m/m}$ mice on a HFD ended up weighing the same as WT mice on a SD. Feeding efficiency, which measures the weight gain per gram food consumed, decreased over time particularly in the $Csb^{m/m}$ mice, indicating an age-associated increase in metabolism (Figure 1B). We therefore investigated the metabolism by housing the mice in metabolic cages and observed increased oxygen consumption rates in $Csb^{m/m}$ mice compared with WT animals under SD (Figures 1C–1E, S1H, and S1I). The increased metabolism in $Csb^{m/m}$ mice was attenuated by a HFD, while the CR $Csb^{m/m}$ mice displayed greatly increased oxygen consumption rates (Figure 1C). Notably, the respiratory exchange ratio (RER) (O_2 consumption / CO_2 production) revealed that $Csb^{m/m}$ mice on a HFD switched completely to β-oxidation, as evident by an RER of ~0.7 (Figure 1D). Heat production was severely decreased in CR mice compared with SD, particularly for the $Csb^{m/m}$ genotype, while the HFD increased the heat production in $Csb^{m/m}$ mice (Figure 1E). In summary, the HFD appeared to normalize the metabolism of $Csb^{m/m}$ mice, while CR exacerbated this phenotype.

No Adverse Effects of a HFD in $Csb^{m/m}$ Mice

A common effect of prolonged ingestion of a HFD is steatohepatitis and diabetes. To investigate these outcomes, we performed oral glucose tolerance tests (OGTTs), measured circulating levels of insulin, and investigated liver histopathology. Interestingly, the HFD $Csb^{m/m}$ mice displayed decreased glucose levels in the OGTT and very low insulin levels as compared to WT mice, indicating well-regulated glucose homeostasis (Figures 1F–1H). Notably, the $Csb^{m/m}$ mice on CR were found to be severely hypoglycemic after only 3 hr fasting and had profound insulin sensitivity, as revealed by the OGTT and low insulin levels (Figures 1F–1H). Histology revealed minimal lipid accumulation in the livers of HFD- and SD-fed $Csb^{m/m}$ mice, in contrast to the SD- and HFD-fed WT mice, who exhibited marked lipid accumulation (Figure 1I).

An effect of the HFD is basal membrane and endothelial thickening and a loss of fenestrations in the liver sinusoid linked to decreased liver endothelial function (Fraser et al., 2012). We therefore performed transmission and scanning electron microscopy (TEM and SEM, respectively). Consistent with the histological results, sinusoidal endothelium appeared thinner in TEM micrographs with less basal membrane thickening in the $Csb^{m/m}$ mice compared with WT mice (Figure S1J, endothelium is labeled e). SEM of SD- and HFD-fed WT mice showed decreased fenestrations, consistent with the fatty liver observed with light microscopy (Figure 1J; a fenestration is indicated by the triangle; sieve plate indicated by the highlighted area; quantification in Figures 1K and 1L). Conversely, SD and HFD $Csb^{m/m}$ mice had preserved endothelium porosity and sieve plate formation, indicating a healthier endothelium relative to the WT mice. Taken together, these data indicate that a HFD rescued the metabolic phenotype of $Csb^{m/m}$ mice without any adverse effects, while CR led to hypoglycemia and an exacerbation of the phenotype in these animals.

A HFD Normalized the Cerebellar and Auditory Neurological Phenotypes of $Csb^{m/m}$ Mice

The cerebellum is severely affected in CS, and thus, we investigated the effect of the diets on this brain region in detail. We started by performing gene expression array to investigate overall changes in the transcriptome. Principal component analysis (PCA) revealed separation of genotypes along principal component 1 (PC1) (x axis, Figure 2A). PC2 (y axis) appeared to describe alterations caused by the diets, since there was no difference in this component between SD-treated WT and $Csb^{m/m}$ mice. Surprisingly, the HFD and resveratrol treatment led to an almost identical transcriptome in both WT and $Csb^{m/m}$ mice, indicating a common target for these interventions (Figures 2A and S2A). When considering the genotype-dependent variability (x axis, PC1), it appeared that the HFD and resveratrol treatment of $Csb^{m/m}$ mice led to a normalization of the genotype effect on the transcriptome. Indeed, the HFD- and resveratrol-treated $Csb^{m/m}$ mice were relatively similar to the CR WT group when performing hierarchical clustering (Figure 2A).

Since the brain does not metabolize fatty acids and a HFD may generate ketone bodies, we speculated that these metabolites may play a role in the transcriptional effects observed. Indeed, circulating levels of β-OHB were moderately increased in the

(J) Representative images of scanning electron microscopy of the sinusoidal endothelium (triangle: fenestration example; highlighted area: sieve plate).
(K) Quantification of the fenestration diameter of the liver sinusoid (n = 4,000–6,000 from three mice in each group, mean ± SD).
(L) The porosity of the liver using the diameter measured in (K) and the total surface area of the endothelium (n = 3, mean ± SEM). See Figure S1 for further information.

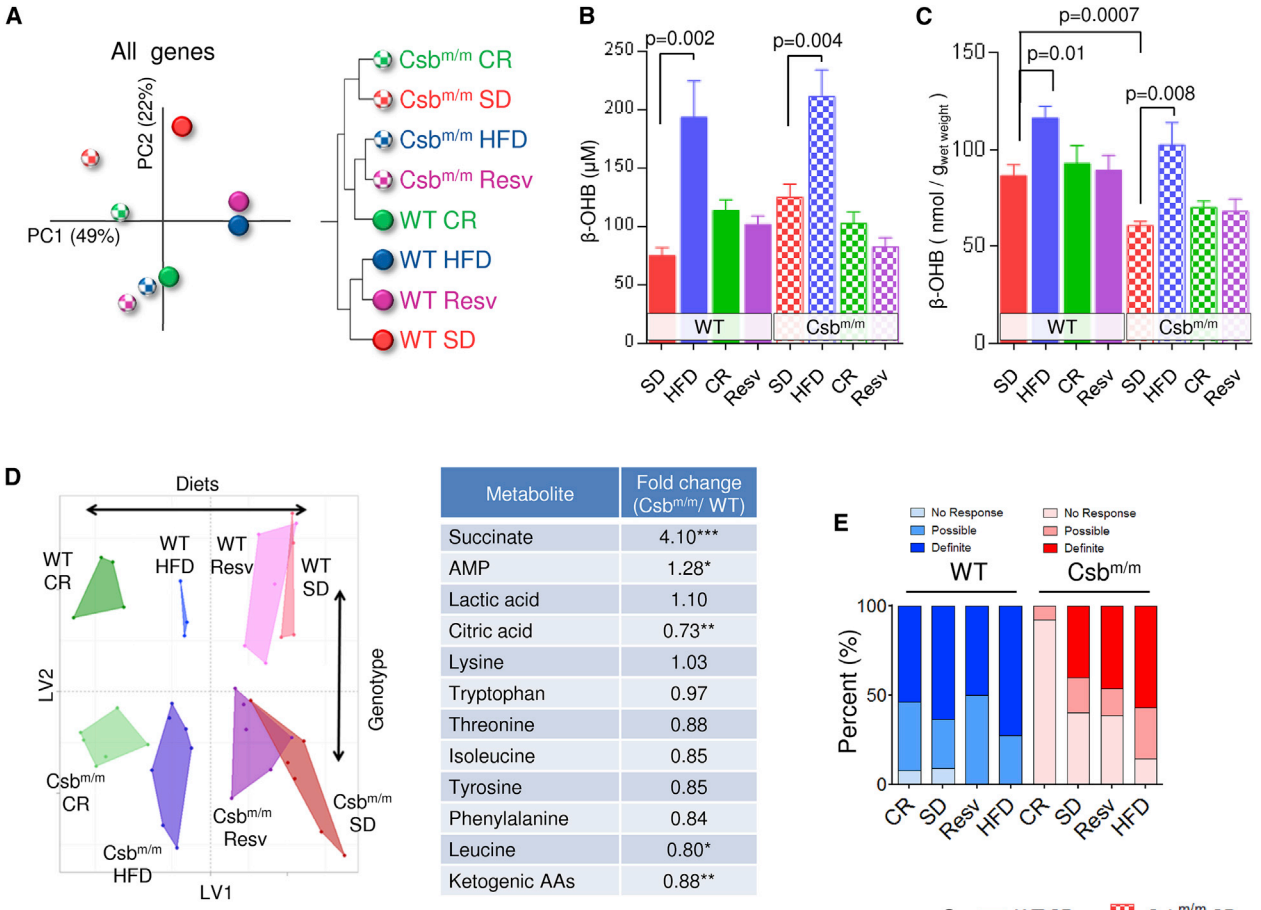

Metabolite	Fold change (Csb$^{m/m}$/ WT)
Succinate	4.10***
AMP	1.28*
Lactic acid	1.10
Citric acid	0.73**
Lysine	1.03
Tryptophan	0.97
Threonine	0.88
Isoleucine	0.85
Tyrosine	0.85
Phenylalanine	0.84
Leucine	0.80*
Ketogenic AAs	0.88**

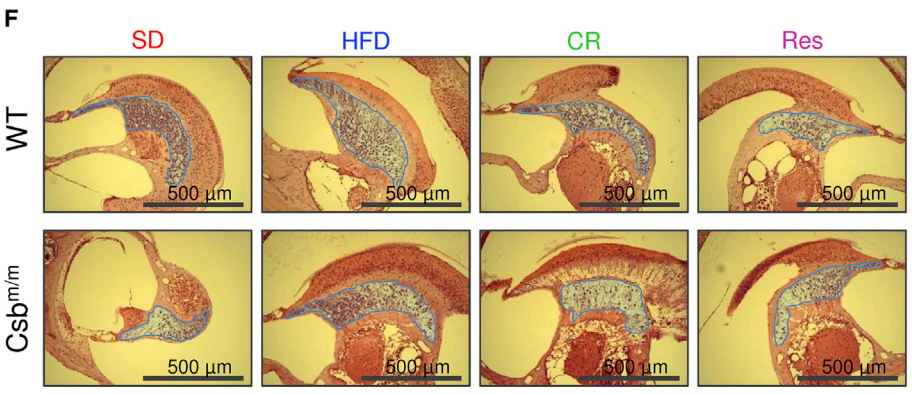

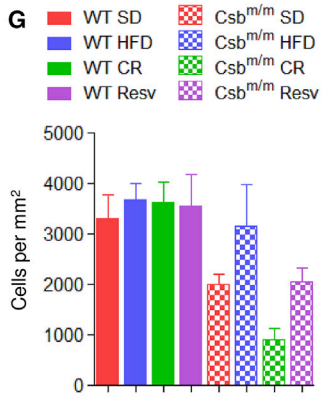

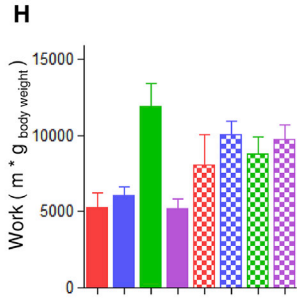

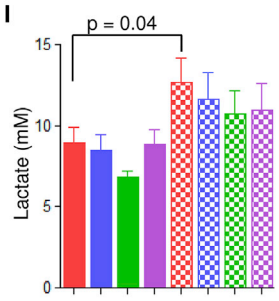

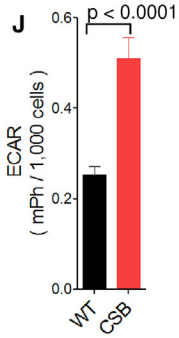

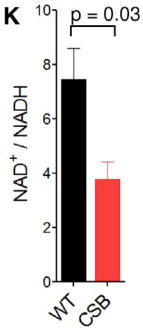

(legend on next page)

HFD-treated mice (Figure 2B). To further understand if these levels of circulating ketones could alter tissue levels of ketone bodies, we proceeded to investigate this in the brain. At the tissue level, β-OHB was significantly decreased in the brain of SD. $Csb^{m/m}$ mice compared with the WT, and the HFD completely rescued this defect (Figure 2C). To further investigate changes in metabolites, we performed untargeted metabolomics analysis on the cerebellum from the mice. Orthogonal partial least-squares regression showed similar effects of a HFD and CR on the entire metabolome of both WT and $Csb^{m/m}$ mice (Figure 2D). However, none of the dietary interventions were able to shift the metabolome of the $Csb^{m/m}$ mice toward WT, indicating that the metabolic alterations in $Csb^{m/m}$ could not be corrected by dietary interventions. Surprisingly, resveratrol had negligible effects on the cerebellar metabolome, perhaps indicating that resveratrol acts by altering the activity of central transcription factors, such as SIRT1, and that the fuel source has a much stronger effect on overall metabolomics compared to transcriptional alterations.

Ketogenic amino acids appeared to be decreased when comparing $Csb^{m/m}$ mice to WT, perhaps indicating an increased ketolysis from amino acids (Figure 2D). Ketones are metabolized in the brain to form acetyl-CoA, a precursor for citrate and myelin synthesis. In agreement with an increase in ketolysis, citrate levels were decreased in the cerebellum (Figure 2D). Ketones, decreases brain inflammation (Jeong et al., 2011) and succinate, an inflammatory marker in the brain (Tannahill et al., 2013), was significantly increased in the cerebellum of $Csb^{m/m}$ mice (Figure 2D). To further investigate the effect of the diets on the cerebellum, we performed TEM on tissue from $Csb^{m/m}$ mice and observed an increased postsynaptic density length after the HFD treatment (Figures S3B and S3C). We assessed cerebellar function utilizing the rotarod and found a better performance of $Csb^{m/m}$ mice compared to WT, which may reflect the large differences in body weight (Figure S2D). In summary, the HFD appears to normalize cerebellar alterations in $Csb^{m/m}$ mice.

Hearing loss is a hallmark feature of CS, aging, and mitochondrial diseases, and we have recently reported an age-associated loss of spiral ganglion cells in $Csb^{m/m}$ mice (Scheibye-Knudsen et al., 2012). To determine the extent of the hearing loss, we performed hearing tests on the mice and assessed the histology of the inner ear. Notably, the HFD protected the $Csb^{m/m}$ mice from age-associated hearing loss at both the behavioral (Figure 2E) and histological levels (Figures 2F and 2G, the spiral ganglion is highlighted in blue in the micrographs). Conversely, the CR $Csb^{m/m}$ mice were deaf and showed extensive loss of spiral ganglion cells. Since the reaction to sound may depend on anxiety levels, we performed open field tests. $Csb^{m/m}$ mice were found to be significantly less anxious than WT mice, a trait anecdotally observed in CS patients. However, there was no difference between CR and HFD groups within the different genotypes, indicating that the loss of an auditory behavioral response was bona fide hearing loss (Figures S3A–S3C).

CSB Deficiency Leads to Lactate Production through a Shift in the NAD/NADH Equilibrium

Sensorineural hearing loss is a common feature in mitochondrial diseases, and mitochondrial dysfunction leads to exercise intolerance and muscle weakness. We therefore investigated the aerobic capacity and muscle strength of $Csb^{m/m}$ mice. Surprisingly, all the $Csb^{m/m}$ mice, except those on CR, ran longer on the treadmill and were stronger than the WT counterparts (Figures 2H, S3D, and S3E). This finding was corroborated when investigating the oxygen consumption rates of isolated mitochondria from the brain and liver of the different animals. Tighter coupled mitochondria were observed in the brain of $Csb^{m/m}$ mice, as indicated by decreased state-4 respiration (no ADP) and an increased coupling ratio after ADP addition, while there were no genotype differences in mitochondria isolated from the liver (Figures S3F–S3K).

Lactate accumulation is a key feature of mitochondrial diseases and is observed in the brain of CS patients (Koob et al., 2010). Due to the increased cerebellar lactate observed in the metabolomics analysis, we measured lactate levels in the serum and found increased levels in $Csb^{m/m}$ mice (Figure 2I). This observation was corroborated in cultured immortalized CSB patient fibroblasts were reconstitution with WT CSB (labeled WT cells) decreased extracellular acidification rates (ECARs) as compared with the empty vector (labeled CSB) reconstituted cells (Figure 2J). Increased lactate production was particularly surprising in light of our finding of increased aerobic performance in the $Csb^{m/m}$ mice and could possibly be explained by a shift in the lactate-pyruvate equilibrium toward lactate. This seemed to be the case at the cellular level when investigating the ability of lactate to stimulate oxygen consumption rates after glycolysis had been inhibited with 2-deoxyglucose. In particular, addition of lactate to WT cells lead to a significant increase in oxygen consumption rates, while a much larger dose of lactate was needed for the same stimulation in CSB cells (Figure S4A). The lactate-pyruvate equilibrium is regulated through

Figure 2. A HFD Increases β-OHB Levels and Rescues the Neurological Phenotype of $Csb^{m/m}$ Mice

(A) A PCA of the unselected average gene expression Z score from the cerebellum and a hierarchical clustering of the same data (n = 3–7).
(B) Levels of circulating β-OHB in the mice (n = 6–12, mean ± SEM).
(C) Levels of β-OHB in the brain of mice (n = 4–9, mean ± SEM).
(D) Orthogonal partial least square regression of metabolomics data done on the same samples as in (D) and a list of some altered metabolites when comparing genotype only. (n = 3–7).
(E) Hearing tests done by exposing the mice to a 108 db recorded clap, videotaping the reaction, and subsequently blindly scoring the mice for a reaction to the sound (n = 10–14).
(F) Representative histological images of hematoxylin-and-eosin-stained sections of the inner ear (blue highlight: spiral ganglion).
(G) Quantification of cells in the spiral ganglion (n = 3, mean ± SEM).
(H) Aerobic capacity of the mice measured by forced treadmill exercise (n = 7–11, mean ± SEM).
(I) Serum lactate levels (n = 7–12, mean ± SEM).
(J) ECARs of immortalized CSB patient cells (CS1AN) reconstituted with WT CSB (WT) or an empty vector (CSB) (n = 28 separate experiments, mean ± SEM).
(K) NAD^+/NADH ratio (n = 3, mean ± SEM).

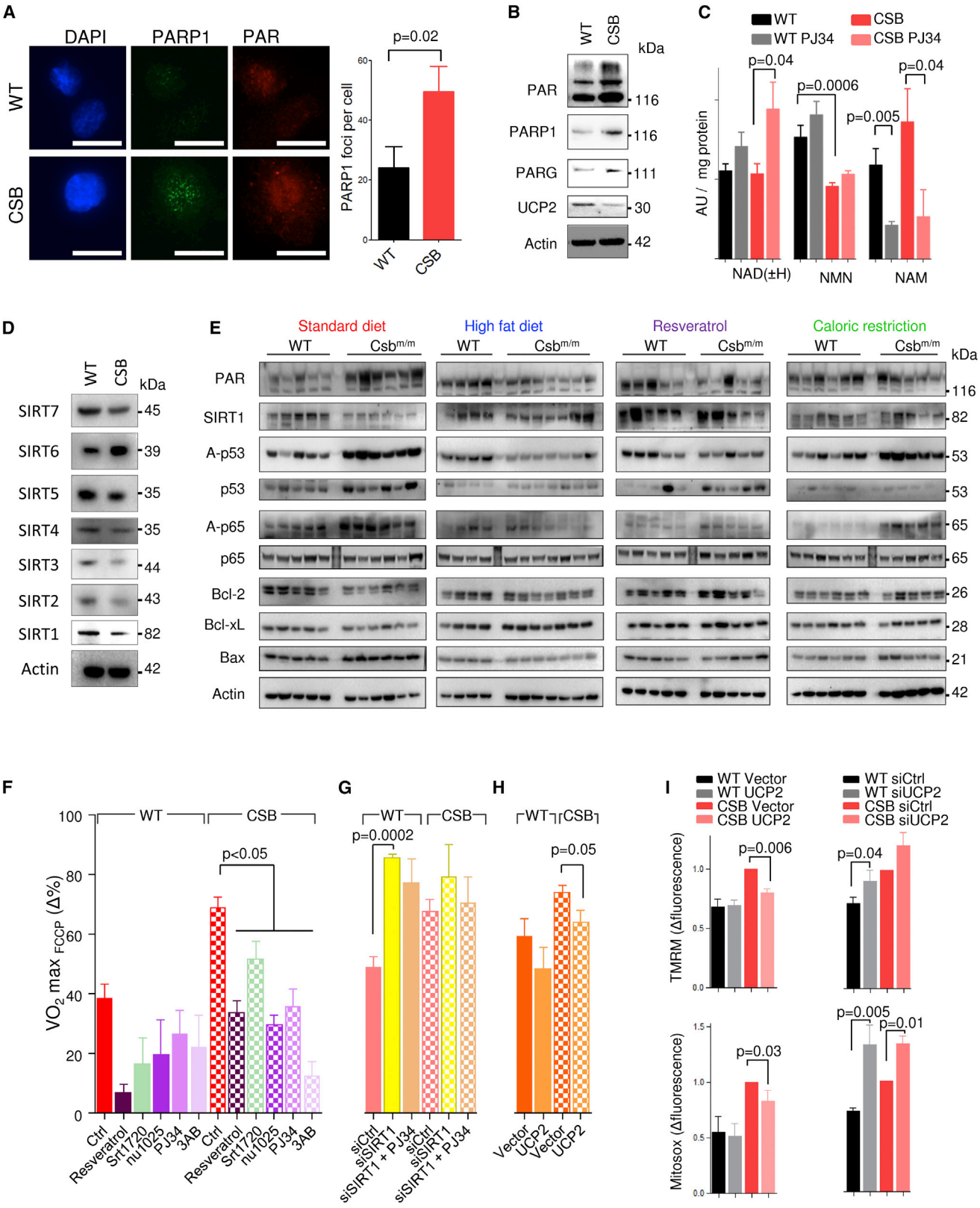

Figure 3. PARP1 Activation Drives SIRT1 Depression and the Mitochondrial Phenotype in CSB-Deficient Cells

(A) Representative confocal microscopy images and quantification of WT and CSB-deficient cells stained for PARP1 and PAR (n = 3, mean ± SEM).

(B) Representative immunoblot of PAR, PARP1, PARG1, and UCP2 in WT and CSB-deficient cells (n = 3, mean ± SEM).

(legend continued on next page)

phosphorylation of the pyruvate dehydrogenase by the pyruvate dehydrogenase kinase (PDK) enzymes. However, we did not find any difference in the expression of PDK1–PDK4 (Figure S4B).

Lactate dehydrogenase uses NADH as a reducing agent, converting it to NAD^+ (Figure S4C). One reason that CSB deficiency increased lactate production could therefore be alterations in the NAD^+/NADH ratio. Indeed, the NAD^+/NADH ratio was decreased in CSB-deficient cells possibly explaining the shift in the lactate-pyruvate equilibrium (Figure 2K). Collectively, our findings suggest that the increased lactate production in CS may result from alterations in the NAD^+/NADH ratio.

PARP Activation Drives SIRT1 Activation in CSB-Deficient Cells and Mice

DNA damage activates PARP1, leading to the formation of PAR polymers and consumption of NAD^+. Since we recently found PARP activation in neurodegenerative DNA repair disorders (Fang et al., 2014), we hypothesized that the defect in repairing DNA damage in CS would lead to NAD^+ depletion, explaining the observed shift in the lactate-pyruvate equilibrium. Indeed, PAR levels and the number of PARP1 foci were higher in CSB-deficient cells than in WT cells (Figures 3A and 3B). Concomitantly, the PAR-degrading enzyme PAR-glycohydrolase (PARG) was increased, possibly indicating greater PAR turnover in CSB-deficient cells (Figure 3B). To further investigate the role of PARP, we performed mass spectrometry on CSB-deficient cells and measured NAD levels as well as metabolites involved in PAR breakdown with and without inhibition of PARP enzymes using PJ34 (Figure 3C). Although we did not find any differences in total NAD levels (the combined concentration of NAD^+ and NADH) between WT and CSB cells, pharmacological inhibition of PARP for 24 hr led to a 2-fold increase in total NAD levels, suggesting much larger recycling of PAR in CSB-deficient cells than in WT (Figure 3C). In addition, the NAD^+ precursor NMN was significantly decreased in CSB-deficient cells (Figure 3C). Nicotinamide, a competitive inhibitor of SIRT1, was increased in CSB-deficient cells. Quite strikingly, PARP inhibition led to a ~60%–80% reduction in nicotinamide levels, indicating that this enzyme is responsible for the majority of cellular nicotinamide production (Figure 3C).

Sirtuins are a family of NAD^+-dependent deacetylases believed to be involved in the aging process (Houtkooper et al., 2012). We therefore investigated the protein levels of the sirtuins and found that all of them, except SIRT6, were decreased in CSB-deficient cells, corresponding with the increased PARP1 activation (Figure 3D). SIRT1 is particularly interesting since it is known to regulate inflammation, apoptosis, and mitochondrial function, parameters that are altered in CS patients and $Csb^{m/m}$ mice. In the cerebellum, PAR levels were increased in SD $Csb^{m/m}$ mice, correlating with the decreased SIRT1 levels. SIRT1 activity was also attenuated, as revealed by the hyperacetylation of p53 and p65 (an NFκB subunit) substrates compared with SD WT mice (Figure 3E). Increased p65 acetylation has been reported to lead to microglial activation and may explain the proinflammatory state in CS (Weidenheim et al., 2009). Furthermore, hyperacetylated p53 could contribute to the increased apoptosis seen in CS. Indeed, proapoptotic BAX was increased while antiapoptotic Bcl-2 and Bcl-xL were decreased in the cerebellum of $Csb^{m/m}$ mice compared with WT animals (Figure 3E). These changes were ameliorated to some extent by the HFD, resveratrol, and CR, indicating common targets in these interventions, perhaps mediated through ketone body metabolism. Taken together, these data suggest that PARP activation leads to SIRT1 attenuation contributing to the proinflammatory and proapoptotic state seen in CS.

PARP-Mediated Attenuation of SIRT1 Leads to Mitochondrial Dysfunction in CS

To test whether PARP1 and SIRT1 could be responsible for the mitochondrial alterations seen in CS, we took advantage of the increase in carbonyl cyanide 4-(trifluoromethoxy) phenylhydrazone (FCCP)-uncoupled respiration seen in CSB-deficient cells compared with WT (Scheibye-Knudsen et al., 2012). The SIRT1 activators, resveratrol and SRT1720, attenuated the increased FCCP-uncoupled respiration in CSB-deficient cells (Figure 3F). The same outcome was achieved with the PARP inhibitors, 3-aminobenzamide (3AB), PJ34, and NU1025 (Figure 3F). Knockdown of SIRT1 rendered both WT and CSB-deficient cells insensitive to PARP inhibition, indicating that SIRT1 acts downstream of PARP activation (Figure 3G). Oxidative DNA lesions can lead to PARP1 activation, and we therefore investigated the effect of culturing the cells in low oxygen. Indeed, incubation in 3% oxygen led to a decrease in FCCP-uncoupled respiration in both WT and CSB-deficient cells (Figure S5A). This effect did not appear to be caused by HIF-1α or HIF-2α activation, since inhibition with LW6 or knockdown of these transcription factors also decreased FCCP-uncoupled respiration (Figure S5A). In addition, the effects of resveratrol were likely not through AMPK, as treatments with the AMPK agonists AICAR and AG769662 or the antagonist dorsomorphin did not lead to any consistent changes (Figure S5A). The relative increase in FCCP-uncoupled respiration could be caused by increased membrane potential. Uncoupling proteins (UCPs) regulate membrane potential, and we recently found that UCP2 was decreased in DNA-repair-deficient diseases (Fang et al., 2014). Indeed, UCP2 levels were decreased in CSB-deficient cells (Figure 3B), and overexpression of exogenous UCP2 significantly decreased FCCP-uncoupled respiration, reduced the

(C) Mass spectrometry of nicotinamide adenine dinucleotide (NAD) and NAD-metabolites in WT and CSB-deficient cells; NMN: Nicotinamide mononucleotide; NAM: Nicotinamide; (n = 6–8, mean ± SEM).
(D) Representative immunoblot of sirtuin levels in WT and CSB-deficient cells.
(E) Immunoblot of protein levels from the cerebellum of WT and $Csb^{m/m}$ mice on various diets. Each lane is a separate mouse.
(F) FCCP uncoupled respiration normalized to basal respiration under various 24 hr treatments (n = 3–28 separate seahorse experiments, mean ± SEM).
(G) FCCP uncoupled respiration normalized to basal respiration 72 hr after SIRT1 siRNA treatment (n = 3, mean ± SEM).
(H) FCCP uncoupled respiration normalized to basal respiration 72 hr after UCP2 overexpression (n = 3, mean ± SEM).
(I) Flow cytometry of WT and CSB-deficient cells after overexpression of UCP2 and stained with tetramethylrhodamine methyl ester (TMRM) for membrane potential and mitosox for mitochondrial superoxide production (n = 3, mean ± SEM).

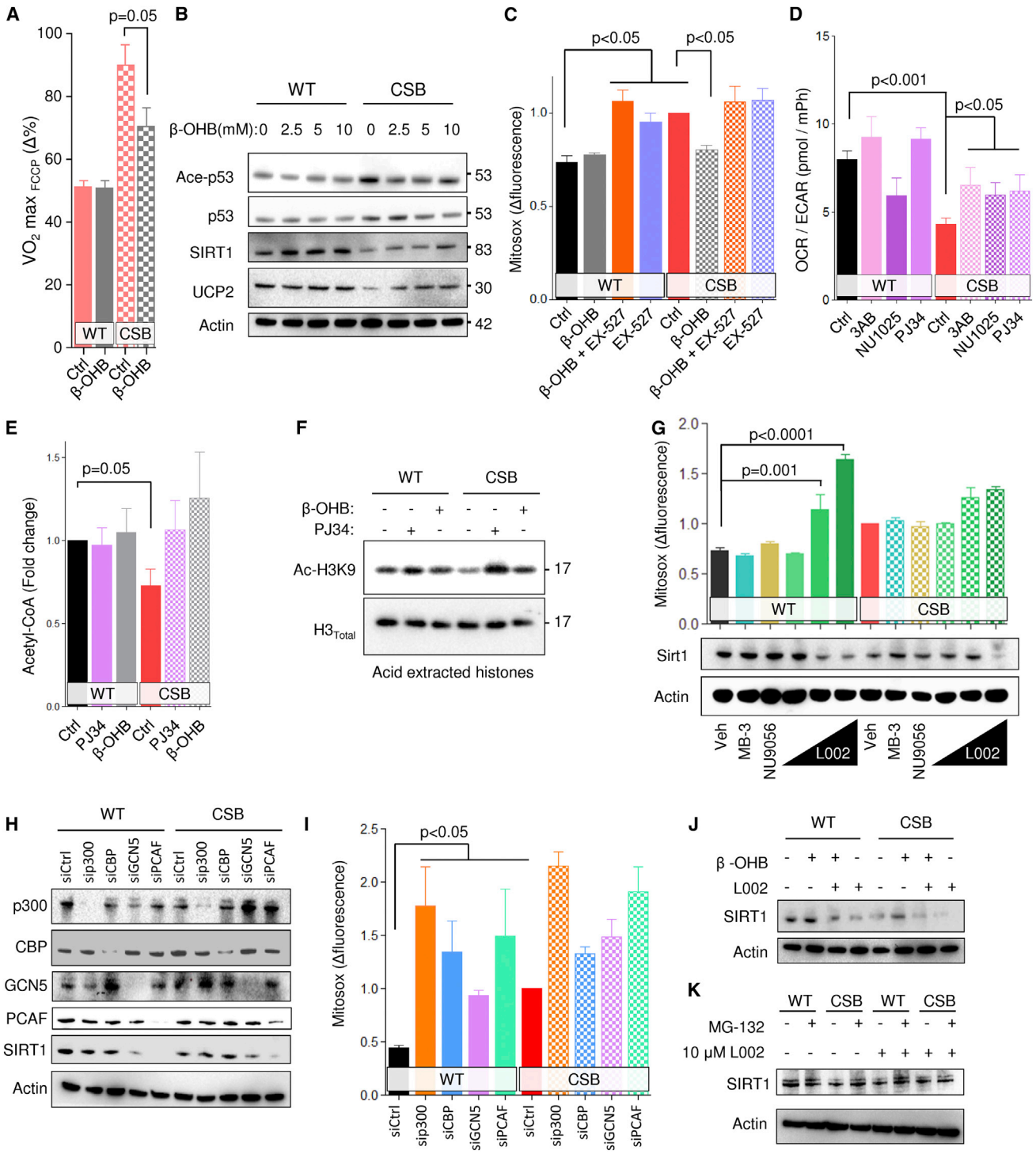

Figure 4. β-OHB and PARP Inhibition Rescues the CS Phenotype through SIRT1 Activation

(A) FCCP uncoupled respiration normalized to basal respiration 48 hr after 10 mM β-OHB treatment (n = 3 separate seahorse experiments, mean ± SEM).

(B) Representative immunoblot of treatment of WT and CSB-deficient cells with increasing concentrations of β-OHB.

(C) Flow cytometry of WT and CSB-deficient cells treated with β-OHB and or EX-527 for 48 hr and stained with mitosox (n = 6, mean ± SEM).

(D) Oxygen consumption rate (OCR) relative to ECAR (n = 3–12 separate seahorse experiments, mean ± SEM).

(E) Acetyl-CoA levels after treatment with the PARP inhibitor PJ34 or β-OHB for 24 hr (n = 6, mean ± SEM).

(F) Representative immunoblot of acid-extracted histones after treatment with the PARP inhibitor PJ34 or β-OHB for 24 hr.

(G) Representative immunoblot from WT and CSB-deficient cells after 24 hr treatment with MB-3, NU9056, or increasing concentration of L002 and flow cytometry of WT and CSB-deficient cells treated with MB-3, NU9056, or increasing concentration of L002 for 24 hr and stained with mitosox (n = 3–12, mean ± SEM).

(legend continued on next page)

membrane potential, and rescued the mitochondrial ROS production in CSB-deficient cells (Figures 3H–3I and S5B for protein levels). In addition, knockdown of UCP2 increased the membrane potential and mitochondrial ROS production in both CSB and WT cells (Figure 3I). Taken together, our data indicate that oxidative stress may lead to PARP1 activation, SIRT1 attenuation, and the mitochondrial phenotype, possibly through loss of UCP2 expression.

Ketone Bodies and PARP Inhibition Rescue the Phenotype of CS through SIRT1 Activation

Since the HFD appeared to increase the levels of ketone bodies, we further investigated the effect of these metabolites in CS. Notably, treatment with β-OHB led to a decrease in FCCP-uncoupled respiration, SIRT1 activation, and increased UCP2 expression in CSB-deficient cells (Figures 4A and 4B). In addition, β-OHB attenuated ROS production and the mitochondrial membrane potential, and this effect appeared to depend upon SIRT1, since its inhibition with EX-527 abolished this effect (Figures 4C and S6A). Interestingly, PARP inhibition using either PJ34 or NU1025 also increased SIRT1 levels, perhaps indicating common pathways between ketone- and PARP-mediated SIRT1 regulation (Figure S6B). Considering β-OHB treatment could increase the intracellular pool of acetyl-CoA, we speculated that PARP inhibition could do the same by changing the lactate/pyruvate equilibrium, thereby increasing the conversion of pyruvate to acetyl-CoA. This appeared to be the case since PARP inhibition increased the OCR/ECAR ratio (Figure 4D). Further, PARP inhibition and β-OHB treatment normalized the acetyl-CoA levels in CSB-deficient cells (Figure 4E). In addition, decreasing flow through glycolysis by incubating the cells in 5 mM glucose led to an increase in FCCP-uncoupled respiration in WT cells, while there was no change in the CSB-deficient cells (Figure S5A). Conversely, incubating cells in oleic acid, which will increase acetyl-CoA levels, normalized the FCCP-uncoupled respiration in CSB-deficient cells (Figure S5A).

Since SIRT1 is a histone deacetylase and acetyl-CoA levels regulate histone acetylation levels, we speculated that there might exist a feedback loop regulating the levels of SIRT1 in response to general histone acetylation levels. Accordingly, β-OHB treatment and PARP inhibition led to increased histone acetylation at sites known to be acetylated after ketone body exposure (Figure 4F) (Shimazu et al., 2013). Histone acetylation is mediated through histone acetyl transferases (HATs). A number of pharmacological HAT inhibitors have been developed: L002, is an inhibitor of p300, CBP, GCN5, and PCAF; NU-9056 inhibits Tip60; MB-3 inhibits GCN5; C646 inhibits P300. Interestingly, WT cells were sensitive (in terms of cell growth) to inhibition by L002, while CS cells were comparatively resistant, indicating that the CSB-deficient cells may have adapted to chronically low activity of HATs inhibited by L002 (Figure S6C). Indeed, L002 treatment led to loss of SIRT1 expression and a similar mitochondrial phenotype in WT cells compared with CSB cells (Figures 4G and S6D). Importantly, inhibition of GCN5 or Tip60 neither altered SIRT1 levels nor lead to changes in mitochondrial function (Figures 4G, S6D, and S6E). There was also no effect on mitochondrial parameters by inhibiting P300 using C646 (Figure S6F). To further understand which HAT may be responsible for alterations in SIRT1 protein levels, we performed knockdown of p300, CBP, GCN5, and PCAF. Notably, knockdown of PCAF, a known interaction partner SIRT1 in the DNA damage response (Pediconi et al., 2009), led to significant loss of SIRT1 protein in WT cells and a strong CS-like mitochondrial phenotype (Figures 4H, 4I, and S6G). Further, the increase in SIRT1 protein levels upon β-OHB appeared to depend on HAT activity, since cotreatment with β-OHB and L002 failed to rescue SIRT1 levels in CSB-deficient cells (Figure 4J). To understand whether the regulation of SIRT1 protein levels happened at the transcriptional level, we measured the activity of the SIRT1 promoter using a luciferase assay and found that at higher concentration L002 treatment appeared to stimulate SIRT1 transcription (Figure S6H). We therefore investigated if the SIRT1 protein stability might be altered by L002 by coincubation with the proteasomal inhibitor MG-132. Indeed, MG-132 treatment rescued the SIRT1 protein levels in CSB-deficient cells as well as in L002-treated WT cells (Figure 4K). In summary, it appears that loss of SIRT1 expression and activity may in part be due to loss of acetyl-CoA levels caused by shunting of glucose to lactate, possibly leading to less PCAF-dependent acetylation activity.

Ketones and PARP Inhibition Are Nonadditive in their Ability to Extend the Lifespan of CSB Nematodes

It has recently been shown that age-associated PARP activation is conserved from nematodes to mammals (Mouchiroud et al., 2013). We therefore investigated this phenomenon in *csb-1* (worm CSB ortholog) mutant worms (*csb-1*). Indeed, PAR levels were significantly increased in the aged *csb-1* worms compared to WT (N2) and young nematodes (Figure 5A). Concomitantly, we observed a decrease in Sir2 (worm SIRT1 ortholog) levels (Figure 5A). Since ketones bodies may be able to reverse some of the phenotypes in human and mouse CS, we asked if β-OHB, PARP, or a combination of these interventions would extend the lifespan in worms. *Csb-1* worms displayed shortened lifespan as compared with N2 (mean lifespan 17.3 days in *Csb-1* versus 19.1 days in N2) and β-OHB treatment, PARP inhibition using PJ34, or a combination of the two, completely rescued this defect in lifespan (Figures 5C–5E). Since the combination treatment did not increase lifespan further than each of the single interventions, the data support the idea that PARP inhibition and ketone bodies may increase lifespan through the same pathway by augmenting acetyl-CoA levels and increasing SIRT1 expression (Figure 5F). In WT N2 worms, neither PJ34 nor β-OHB led to lifespan extension (Figures 5G and 5H); however, the combined treatment did lead to a slight but significant increase in N2 lifespan (Figure 5I). Nonetheless, there was no significant difference when comparing each of the interventions, indicating that the same pathway may be activated by these

(H) Representative immunoblot of protein levels after knockdown of various proteins.
(I) Flow cytometry of WT and CSB-deficient cells subjected to siRNA knockdown of various proteins and stained with mitosox (n = 3, mean ± SEM).
(J) Representative immunoblot of protein levels after treatment with L002 and/or β-OHB.
(K) Representative immunoblot of protein levels after treatment with L002 and/or MG-132.

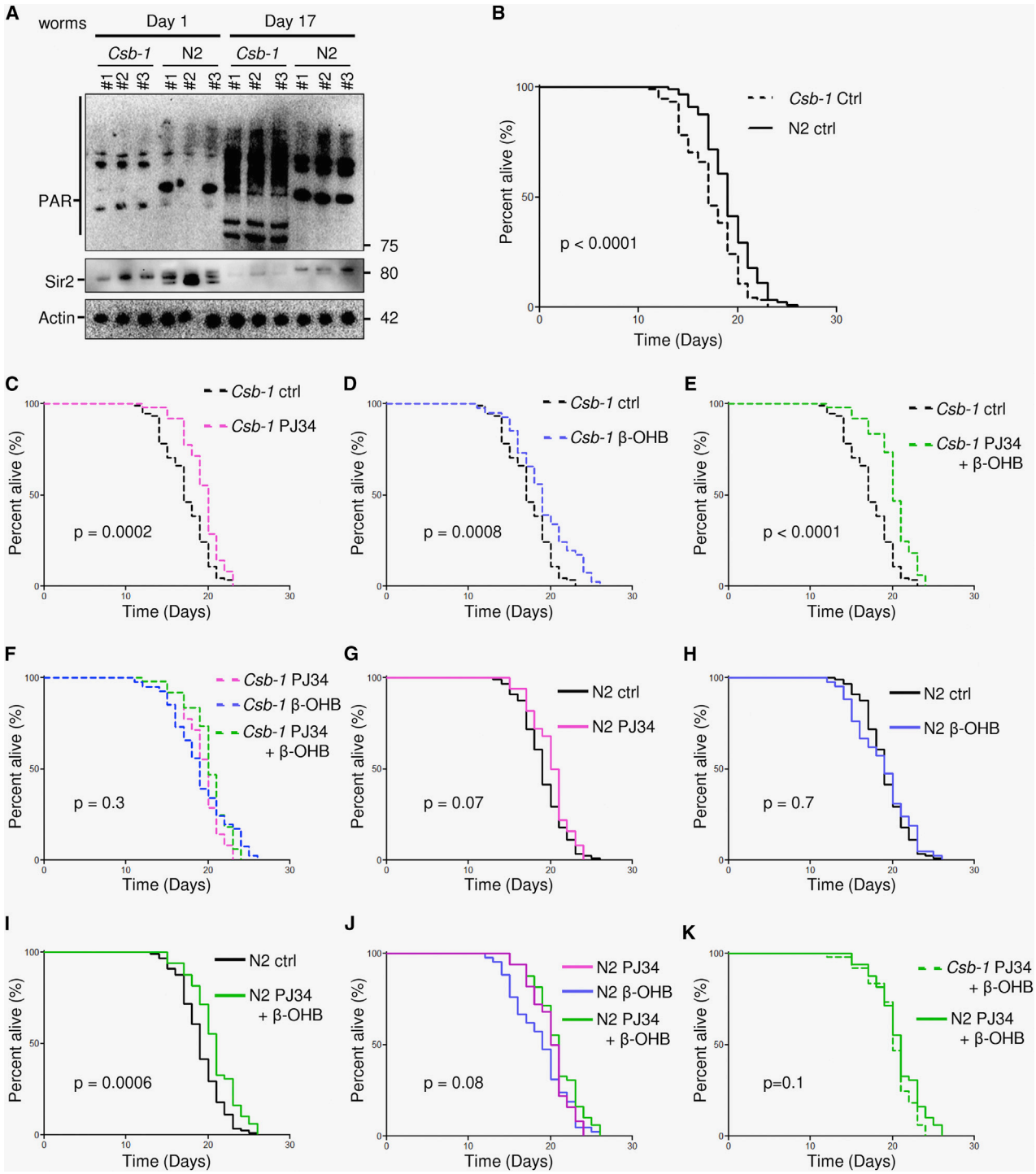

Figure 5. The Longevity Effect of β-OHB and PARP Inhibition Are Nonadditive in Short-Lived csb-1 Nematodes

(A) Representative immunoblot from old and young *csb-1* and N2 worms. Each lane represents a separate worm cohort.

(B) Kaplan-Meier survival curves of *csb-1* and N2 nematodes (n = 100).

(C) Survival curves of *csb-1* nematodes treated with 0.1 μM PJ34 (n = 50).

(D) Survival curves of *csb-1* nematodes treated with 25 mM β-OHB (n = 50).

(E) Survival curves of *csb-1* nematodes treated with 0.1 μM PJ34 and 25 mM β-OHB (n = 50).

(F) Survival curves of *csb-1* nematodes treated with 0.1 μM PJ34, 25 mM β-OHB, or 0.1 μM PJ34 and 25 mM β-OHB (n = 50).

(G) Survival curves of WT N2 nematodes treated with 0.1 μM PJ34 (n = 50).

(legend continued on next page)

compounds (Figure 5J). Interestingly, the lifespan of the *csb-1* and N2 worms on the combination treatment was identical (Figure 5K).

CSB Is Retained at DNA Damage Sites by PAR to Displace PARP1 from DNA

Considering that PARP1 inhibition appeared to attenuate the CS phenotype and that CSB is known to interact with PARP1 (Thorslund et al., 2005), we investigated the functional relationship between these proteins in greater detail. CSB has previously been shown to displace proteins from DNA (Berquist and Wilson, 2009), and we therefore speculated that CSB may interact with and/or modulate PARP1 on DNA. Consistent with this notion, a different binding pattern was observed in an electrophoretic mobility shift assay of the PARP1-DNA complexes when incubated with CSB (Figure 6A). To further characterize this phenomenon, we examined the ability of CSB to displace PARP1 from a BamH1 restriction-site-containing DNA duplex. Interestingly, CSB was only able to displace PARylated PARP1 and not unmodified PARP1 (shown by increased BamH1 cleavage of the DNA), indicating that PARP1 has to be activated before it can be removed from DNA (Figure 6B). In support of this idea, recombinant CSB decreased the DNA-dependent ribosylation activity of PARP1 in the presence of UV-damaged DNA in vitro (Figure 6C). It was recently shown that UV radiation can activate PARP1 (Robu et al., 2013). To test if CSB would modulate the activity of PARP in vivo, we irradiated cells with 5 J/m^2 and measured the activation of PARP over time. Indeed, UV damage led to a modest activation of PARP in the WT cells over time. In CSB-deficient cells, PARP was strongly activated, and the activation persisted, supporting the idea that CSB participates in the removal of PARP on damaged DNA (Figure 6D).

Since PARylation status apparently modulated the activity of CSB, we measured the recruitment of CSB to laser-induced DNA damage after PARP inhibition. We observed that CSB recruitment was independent of PARP activation, whereas retention of CSB at the site of damage was influenced by PAR polymers (Figure 6E). Indeed, CSB appeared to have an extraordinary strong ability to bind PAR noncovalently in vitro, as demonstrated by far-western and slot blot assays. Here, far-western showed increasing PAR binding with increasing CSB loaded (Figure S6I). We confirmed the results using slot blot showing dose-dependent PAR binding to CSB (Figure 6F; histone H1 is a positive control; BSA is a negative control). In support of this, two conserved PAR binding motifs (Pleschke et al., 2000) were identified in the N-terminal PARP1 binding region of CSB, and mutating the lysines to alanines in these sites led to loss of retention of CSB at the damage (Figures 6G and 6H). Further, CSB retention in PARP1 null HeLa cells was also decreased, supporting the role of PAR binding in the retention of CSB at the damage (Figure 6I). Thus, CSB may be retained at DNA damage through interactions with PARylated proteins and facilitate the removal of PARylated PARP1 from the DNA to enable downstream DNA repair to occur.

PARP Inhibition or NAD^+ Replenishment Rescues the Mitochondrial Phenotype in CS

Since PARP activation appeared to drive much of the phenotype in CS, we asked whether inhibition of this enzyme could rescue the mitochondrial dysfunction. Accordingly, treatment with 3AB, NU1025, and PJ34 led to a significant decrease in oxygen consumption in CSB-deficient cells compared with WT cells, perhaps indicating that PARP activation drives increased ATP consumption in CSB-deficient cells (Figure 7A). Further, 24 hr treatments with these inhibitors decreased the mitochondrial ROS production in CSB-deficient cells (Figure 7B). PJ34 has shown anti-inflammatory and neuroprotective properties in vivo (Hamby et al., 2007). We therefore investigated the effect of this compound on the metabolism of $Csb^{m/m}$ mice by daily intraperitoneal injections while housing the mice in metabolic cages. As expected, PJ34 treatment decreased oxygen consumption rates over time in old $Csb^{m/m}$ and to some extent in old WT mice, whereas young mice of either genotype showed no effect of this compound (Figure 7C). These data suggest that an age-related increase in DNA damage may drive the hypermetabolic phenotype in CS.

Supplementation with NAD^+ precursors have recently been shown to recover defects caused by age-associated increases in PARP activation (Gomes et al., 2013; Mouchiroud et al., 2013). We therefore treated old and young $Csb^{m/m}$ mice with nicotinamide riboside (NR). As expected, old $Csb^{m/m}$ mice had decreased NAD^+ and ATP levels before the treatment. Remarkably, a single week of treatment with NR completely normalized these levels (Figures 7D and 7E). Furthermore, isolated cerebellar mitochondria from $Csb^{m/m}$ mice show increased membrane potential as well as ROS production, and NR treatment rescued these defects (Figures 7F–7I). Because increasing NAD^+ levels should activate transcription factors, we next isolated RNA from the cerebellum of the old and young WT and $Csb^{m/m}$ mice and performed microarray studies. PCA of the average Z scores of the entire data set revealed separation of old and young mice along PC1 (x axis) that accounted for 43% of the total variability among the data sets (Figure 7J). Notably, saline-treated $Csb^{m/m}$ mice were furthest to the left on PC1, supporting the idea that this mouse model may indeed represent an accelerated aging model. Importantly, NR treatment resulted in a normalization of the cerebellar transcriptome in the old $Csb^{m/m}$ mice (Figure 7K). This was supported by examining individual gene expression data where 370 genes were significantly changed when comparing saline-treated old $Csb^{m/m}$ mice versus to WT mice, and only 173 genes were significantly changed when comparing NR-treated old $Csb^{m/m}$ mice to old WT mice (Figure 7K). The same was observed when looking at significantly changed gene ontology terms, where saline-treated

(H) Survival curves of WT N2 nematodes treated with 25 mM β-OHB (n = 50).
(I) Survival curves of WT N2 nematodes treated with 0.1 μM PJ34 and 25 mM β-OHB (n = 50).
(J) Survival curves of WT N2 nematodes treated with 0.1 μM PJ34, 25 mM β-OHB, or 0.1 μM PJ34 and 25 mM β-OHB (n = 50).
(K) Survival curves of WT N2 and *csb-1* nematodes treated 0.1 μM PJ34 and 25 mM β-OHB (n = 50).

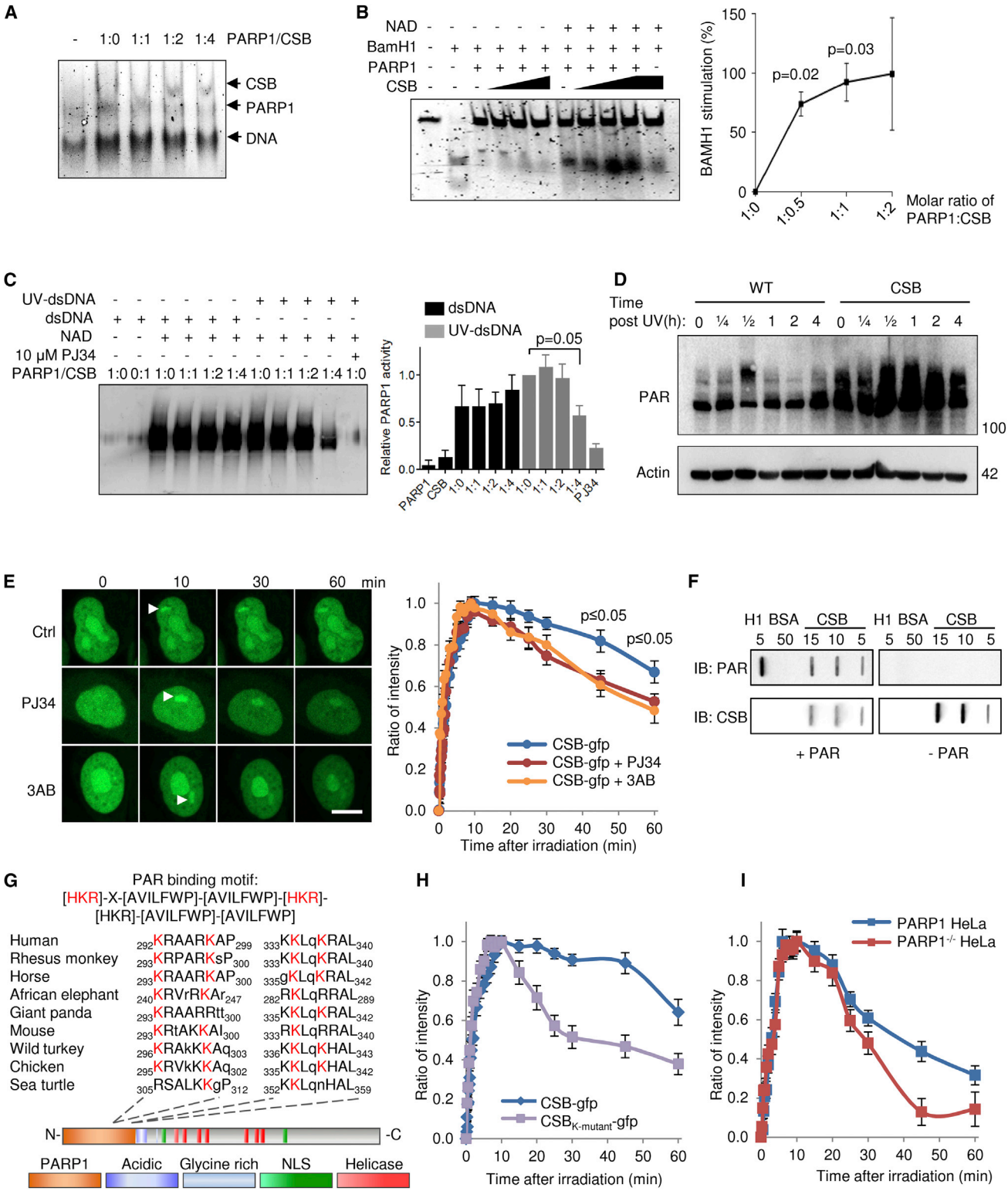

Figure 6. CSB Inhibits PARP1 Activation In Vitro and In Vivo through Displacement of PARylated PARP1 from DNA

(A) Electromobility shift assay (EMSA) of PARP1 and CSB binding to double-stranded DNA.

(B) BamH1 incision of a 42-mer oligo preincubated with 250 nM PARP1 and with increasing amounts of CSB with or without NAD^+ (n = 3, mean ± SEM).

(C) Representative immunoblot and quantification of in vitro poly-ADP-ribosylation (PARylation) of CSB and PARP1. Reactions were performed with recombinant proteins in the presence of undamaged or damaged DNA (n = 3, mean ± SEM).

(legend continued on next page)

old $Csb^{m/m}$ mice versus WT had 213 significantly changed terms, while NR-treated $Csb^{m/m}$ mice versus WT only had 110 changed pathways (Figure 7L). Interestingly, looking closer at the GO terms that were corrected by NR treatment revealed complete normalization of the mitochondrial pathways, as well as normalization of terms involved in oxidative stress, transcription, DNA repair, DNA damage response, and histone acetylation (Tabel S1). In summary, PARP inhibition or NAD^+ replenishment appears to rescue the CS-associated phenotypes in human cells and mice, supporting the role of PARP activation in the pathogenesis of this disorder.

DISCUSSION

We found that a HFD rescues neurological and metabolic phenotypes of a mouse model of the accelerated aging disorder CS. CSB deficiency leads to PARP1 activation, NAD^+ depletion, and attenuation of SIRT1. The HFD did not alter glucose homeostasis but moderately increased the levels of the circulating ketone β-OHB. PARP1 inhibitors or β-OHB treatment also rescue lifespan defects in csb-1 nematodes and mitochondrial defects in CSB-deficient human cells. This may occur through acetyl-CoA-mediated activation of PCAF leading to increased expression of SIRT1. CSB is able to remove PARylated PARP1 from DNA and inhibit its polymerization activity in the presence of damaged DNA. CSB is recruited to sites of DNA damage through transcription (Menoni et al., 2012) but may be retained at the lesion by binding to the PAR-polymer. We propose that once at the site of DNA damage, CSB is retained by PAR and subsequently removes PARylated PARP1 to allow downstream repair to occur. In total, loss of CSB may lead to mitochondrial dysfunction and a proinflammatory and proapoptotic state by hyperactivation of PARP1 and SIRT1 attenuation.

Several theories regarding the pathogenesis of CS have evolved. These include roles for CSB in basal transcription, as well as two central DNA repair pathways, namely, transcription-coupled nucleotide excision repair and base excision repair (Scheibye-Knudsen et al., 2013a). Transcription-coupled nucleotide excision repair is a versatile pathway that deals with a large number of lesions that are able to stall RNA polymerases. It has been proposed that CSB and CSA participate in the ubiquitination of a stalled RNA polymerase (Hanawalt and Spivak, 2008). This may facilitate either the removal or backtracking of the polymerase from the DNA lesion to allow downstream repair processes to occur. In addition, CSB has been implicated in base excision repair, the pathway that deals with single-base lesions often caused by oxidative stress (Scheibye-Knudsen et al., 2013a). Notably, PARP1 plays a major role in this pathway. We now propose that CSB recruitment to DNA damage is dependent on transcription, while retention depends on PARP activation. Our study thereby suggests that there may be a crosstalk between base excision repair and transcription that could be central in the pathogenesis of CS.

$Csb^{m/m}$ mice represents a reasonable model for mild human CS and thus potentially for neuronal aging. Like the $Csb^{m/m}$ mouse, human CS patients have increased lactate production, which may be a result of increased PARP activation, loss of NAD^+, alterations in the lactate/pyruvate ratio, and decreased levels of acetyl-CoA. The pleiotropic effects on the metabolism of alterations in NAD^+ could be profound. For example, fatty acid synthesis is dependent on acetyl-CoA, and the loss of fat mass, as is reported in CS patients and $Csb^{m/m}$ mice, could be a result of decreased shunting of glucose to acetyl-CoA. Similarly, leukodystrophy is prevalent in CS patients, and loss of acetyl-CoA could lead to defects in myelin synthesis. Further, recycling of NAD^+ is energetically expensive with a cost of 4 ATP-equivalents for each NAD^+ molecule metabolized. Our data suggest that PARP may be a factor driving the relative increased energy consumption seen with age in $Csb^{m/m}$ mice. The increased energy consumption could account for the maintained glucose homeostasis in the HFD-treated $Csb^{m/m}$ mice. In addition, a shift in the lactate/pyruvate ratio could lead to decreased glucose utilization in the mitochondria where the HFD could supply acetyl-CoA necessary for oxidative phosphorylation. Although speculative, this could lead to the decrease in RER observed in the HFD-treated $Csb^{m/m}$ mice.

Mitochondrial maintenance may be central in the aging process, and interventions that preserve mitochondrial function appear to extend the lifespan of model organisms. Ketones are known to increase mitochondrial biogenesis and the expression of UCPs (Bough et al., 2006; Sullivan et al., 2004). Importantly, SIRT1 is known to regulate both these factors through activation of downstream transcription factors such as PGC-1α (Houtkooper et al., 2012). In fact, the PGC-1 family of transcription factors was first discovered as regulators of UCP expression (Puigserver et al., 1998). Here, we show that SIRT1 and UCP2 expression is activated by ketones in CSB-deficient cells, perhaps explaining some of the effect of the ketogenic diet on mitochondrial health. Further, it appears that PARP inhibition and ketone body treatment are nonadditive in their ability to extend the lifespan of *Csb-1* worms, indicating that they work in the same pathway. Although somewhat speculative, the transcriptomic data on the diet-treated mice support this hypothesis, since mice treated with resveratrol or the HFD show similar gene expression profiles in the cerebellum. We should, however, note that the HFD could affect the cerebellum in other ways than merely through increased ketone levels. Nevertheless, our combined results imply that these interventions converge on the same central transcription factor: SIRT1.

Ketone bodies as well as triglycerides are hydrolyzed to yield acetyl-CoA molecules. Increasing acetyl-CoA levels alter the epigenetic landscape through stimulation of histone acetylation

(D) Representative immunoblot of whole cell (PARylation) after 5 J/m^2 treatment in WT and CSB-deficient cells at various time points.
(E) Recruitment of GFP-tagged CSB to laser-induced DNA damage after 1 hr preincubation with PARP inhibitors 3AB or PJ34.
(F) Representative slot-blot showing noncovalent interaction between CSB and PAR.
(G) The PAR binding motif in CSB.
(H) Recruitment to laser-induced DNA damage of GFP-tagged WT CSB or CSB harboring K to A mutations in the four conserved lysines.
(I) Recruitment of GFP-tagged WT CSB to laser-induced DNA damage in WT HeLa or *PARP1*$^{-/-}$ HeLa cells.

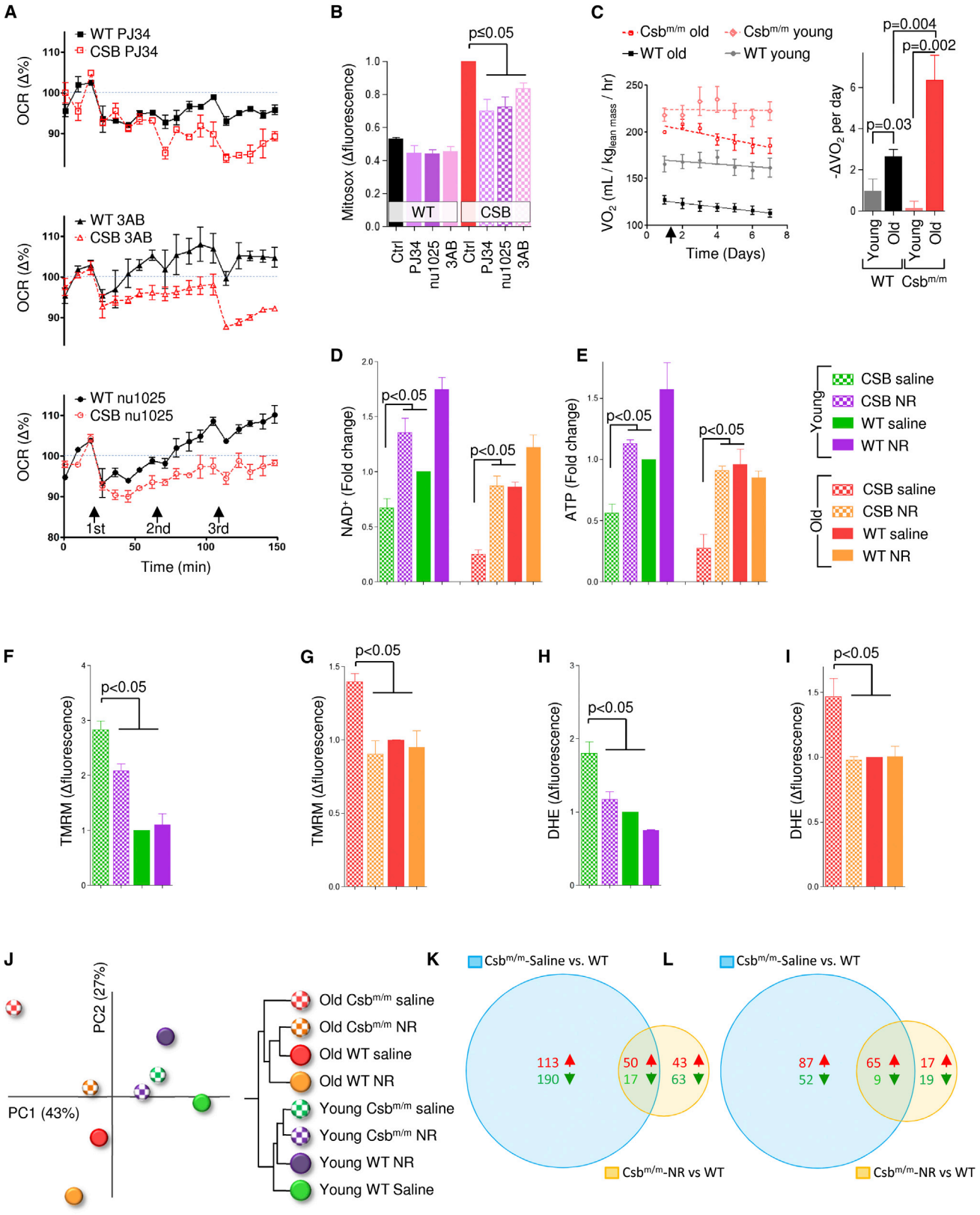

Figure 7. PARP Inhibition or NAD⁺ Replenishment Rescues CS-Associated Alterations in Mice and Human Cells

(A) Measurements of the oxygen consumption rate using the Seahorse XF24 analyzer while adding increasing doses of the PARP inhibitors 3AB, NU1025, or PJ34 (n = 3 separate experiments, mean ± SEM).

(legend continued on next page)

(Sutendra et al., 2014). This may be pertinent under conditions where acetyl-CoA levels are low as in CS. Histone acetylation can act as a positive regulator of transcription, and this is particularly relevant for CS. A hallmark feature of CS cells is the inability to resume RNA synthesis after UV-irradiation as well as an overall decreased level of transcription (Mayne and Lehmann, 1982). These observations led to the idea that CSA and CSB may be transcription factors that are part of the general transcriptional machinery (Lainé and Egly, 2006). The current evidence implies that DNA damage leads to decreases in NAD^+ levels, the lactate-pyruvate ratio, and total acetyl-CoA levels, which in turn leads to decreased overall histone acetylation and consequently inhibition of transcription. Since PARP is persistently activated upon DNA damage in CS, this could perhaps explain the failure to resume RNA synthesis after UV irradiation.

In closing, our findings provide evidence of a nuclear-mitochondrial crosstalk in CS that centers on persistent activation of a DNA damage response through PARP1 and a concomitant decrease in NAD^+ and acetyl-CoA levels. Accordingly, interventions that increase the NAD^+ or acetyl-CoA rescue CS-related phenotypes, thereby representing novel treatments for this incurable accelerated aging syndrome.

EXPERIMENTAL PROCEDURES

Animals

Four-month-old mice were fed a standard AIN-93G diet (SD; carbohydrate:protein:fat ratio of 64:19:17 percent of kcal) ad libitum or at 40% CR, a SD-supplemented with 100 mg/kg_{chow} resveratrol ad libitum, or a HFD ad libitum consisting of AIN-93G with 60% of calories from fat, primarily hydrogenated coconut oil (HFD; carbohydrate:protein:fat ratio of 16:23:61). WT and $Csb^{m/m}$ are on a C57Bl6 background. All measurements were done at 1 year of age. Unless otherwise stated, blood samples were collected after 6 hr of fasting at approximately 6 hr into the light cycle. Body weight and food intake were monitored every other week. Animal rooms were maintained at ~20°C and a 12 hr light/dark cycle. All animal protocols were approved by the Animal Care and Use Committee (352-LEG-2012) of the National Institute on Aging.

Metabolic Assessment

Metabolic rate of the mice was assessed by indirect calorimetry in open-circuit oxymax chambers using the Comprehensive Lab Animal Monitoring System (CLAMS; Columbus Instruments, Columbus). For PJ34 injection experiments mice were acclimatized to monitoring cages for 3 days where daily saline injections were given. Body composition was measured using nuclear magnetic resonance spectroscopy before and after starting the experiment.

Cell Culture

SV40-transformed CS1AN cells stably transfected with either CSB (WT CSB) or empty vector were cultured in Dulbecco's modified Eagle's medium (DMEM) supplemented with 10% FBS, 1% pen-strep, and 400 μg/ml geneticin and grown in 20% O2/5% CO2 at 37°C. PARP1 knockout HeLa cells were a kind gift of A. Mangerich, A. Bürkle, and E. Ferrando-May. Treatments done: resveratrol 100 μM for 48 hr; Srt1720 3 μM for 48 hr; NU1025 100 μM for 48 hr; PJ34 10 μM for 48 hr; 3AB 1 mM for 48 hr; β-OH-butyrate 10 mM for 48 hr; A-769662 10 μM for 48 hr; AICAR 1 mM for 48 hr; Dorsomorphin 5 μM for 48 hr; 3%O_2 treatment 72 hr; LW6 2.5/5 μM for 48 hr; siRNAs for 72 hr; 0.5 mM Oleic acid for 72 hr; 5 mM glucose for 72 hr; 100 μM EX-527 for 24 hr; 5/10/20 μM L002 for 24 hr; 50 μM MB-3 for 24 hr; 10 μM NU9056 for 24 hr; 5 μM C646 for 24 hr; 10 μM MG-132 for 5 hr.

Oxygen Consumption

Oxygen consumption and ECAR measurements were performed using the Seahorse XF-24 instrument (Seahorse Biosciences, North Billerica). Oxygen consumption in isolated mitochondria was done in the Oroboros oxygraph (Oroboros, Innsbruck, Austria).

NAD, Ketones, and Acetyl-CoA Measurements

Performed using either commercially available kits or through liquid chromatography-tandem mass spectrometry.

Nematode Studies

Bristol N2 (WT) and csb-1 worms (ok2335) were outcrossed five times to the N2 prior to use. Lifespan analysis was performed at 25°C on classical NGM plates, or NGM plates supplemented with 25 mM β-OHB seeded with *E. coli* OP50 as food source. 25 L4 stage worms (Day 0) were transferred to two plates, to give synchronous populations of 50 animals per condition. Animals were scored as dead or alive and transferred every day to fresh plates during the fertile period.

Flow Cytometry

Cells were washed in PBS once and trypsinized. Cells were then resuspended in DMEM without phenol red supplemented with 10% FBS containing 50 nM mitotracker Green FM (Invitrogen, Carlsbad), 20 nM TMRM (Invitrogen, Carlsbad), 3 μM dihydroethidium (Invitrogen, Carlsbad), or 3 μM mitosox (Invitrogen, Carlsbad).

See Supplemental Experimental Procedures for detailed methodologies.

SUPPLEMENTAL INFORMATION

Supplemental Information includes six figures, one table, and Supplemental Experimental Procedures and can be found with this article online at http://dx.doi.org/10.1016/j.cmet.2014.10.005.

ACKNOWLEDGMENTS

We are grateful to Dawn Nines, Dawn Phillips, and Justine Lucas for their excellent animal care. We thank Dr. Alexander Bürkle for discussion and critical reading of the manuscript. We thank Elisa Ferrando-May (University of Konstanz) for the kind gift of HeLa *PARP1*$^{-/-}$ cells. S.J.M. was supported by a National Medical Health and Research Council of Australia CJ Martin Early Career Fellowship (RGMS ID 2010-01671). S.V. was supported by a fellowship of the DFG-funded Research Training Group 1331. A.M. was supported by the Zukunftskolleg Konstanz. Funding was provided by the Intramural Research Program of the NIA/NIH.

(B) Flow cytometry of mitochondrial superoxide production in WT and CSB-deficient cells after 24 hr treatment with the PARP inhibitors (n = 3, mean ± SEM).
(C) Whole-body oxygen consumption rates in 4-month-old (young) and 16-month-old (old) WT and $Csb^{m/m}$ mice after daily intraperitoneal injections of PJ34 (25 mg/kg body weight) (n = 3–8, right is the quantification of the slopes).
(D and E) NAD^+ and ATP levels in the cerebellum of young and old WT and $Csb^{m/m}$ mice after 1 week treatment with the NAD^+ precursor NR (n = 3–5, mean ± SEM).
(F–I) Membrane potential and ROS production in isolated mitochondria from the cerebellum of WT and $Csb^{m/m}$ mice (n = 3–5, mean ± SEM).
(J) A PCA and hierarchical clustering of transcriptomic changes in the cerebellum of mice treated with NR.
(K) Venn diagram of significantly changed gene expressions when comparing old $Csb^{m/m}$ saline-treated mice versus old WT saline-treated mice and old $Csb^{m/m}$ NR-treated mice versus old WT saline.
(L) Venn diagram of significantly changed gene expressions when comparing old $Csb^{m/m}$ saline-treated mice versus old WT saline-treated mice and old $Csb^{m/m}$ NR-treated mice versus old WT saline.

Received: April 15, 2014
Revised: July 12, 2014
Accepted: October 6, 2014
Published: November 4, 2014

REFERENCES

Berquist, B.R., and Wilson, D.M., 3rd. (2009). Nucleic acid binding activity of human Cockayne syndrome B protein and identification of Ca(2+) as a novel metal cofactor. J. Mol. Biol. *391*, 820–832.

Bough, K.J., Wetherington, J., Hassel, B., Pare, J.F., Gawryluk, J.W., Greene, J.G., Shaw, R., Smith, Y., Geiger, J.D., and Dingledine, R.J. (2006). Mitochondrial biogenesis in the anticonvulsant mechanism of the ketogenic diet. Ann. Neurol. *60*, 223–235.

Fang, E.F., Scheibye-Knudsen, M., Brace, L.E., Kassahun, H., SenGupta, T., Nilsen, H., Mitchell, J.R., Croteau, D.L., and Bohr, V.A. (2014). Defective mitophagy in XPA via PARP-1 hyperactivation and NAD(+)/SIRT1 reduction. Cell *157*, 882–896.

Fraser, R., Cogger, V.C., Dobbs, B., Jamieson, H., Warren, A., Hilmer, S.N., and Le Couteur, D.G. (2012). The liver sieve and atherosclerosis. Pathology *44*, 181–186.

Gomes, A.P., Price, N.L., Ling, A.J., Moslehi, J.J., Montgomery, M.K., Rajman, L., White, J.P., Teodoro, J.S., Wrann, C.D., Hubbard, B.P., et al. (2013). Declining NAD(+) induces a pseudohypoxic state disrupting nuclear-mitochondrial communication during aging. Cell *155*, 1624–1638.

Hamby, A.M., Suh, S.W., Kauppinen, T.M., and Swanson, R.A. (2007). Use of a poly(ADP-ribose) polymerase inhibitor to suppress inflammation and neuronal death after cerebral ischemia-reperfusion. Stroke *38*, 632–636.

Hanawalt, P.C., and Spivak, G. (2008). Transcription-coupled DNA repair: two decades of progress and surprises. Nat. Rev. Mol. Cell Biol. *9*, 958–970.

Houtkooper, R.H., Pirinen, E., and Auwerx, J. (2012). Sirtuins as regulators of metabolism and healthspan. Nat. Rev. Mol. Cell Biol. *13*, 225–238.

Jeong, E.A., Jeon, B.T., Shin, H.J., Kim, N., Lee, D.H., Kim, H.J., Kang, S.S., Cho, G.J., Choi, W.S., and Roh, G.S. (2011). Ketogenic diet-induced peroxisome proliferator-activated receptor-γ activation decreases neuroinflammation in the mouse hippocampus after kainic acid-induced seizures. Exp. Neurol. *232*, 195–202.

Jucker, M. (2010). The benefits and limitations of animal models for translational research in neurodegenerative diseases. Nat. Med. *16*, 1210–1214.

Koob, M., Laugel, V., Durand, M., Fothergill, H., Dalloz, C., Sauvanaud, F., Dollfus, H., Namer, I.J., and Dietemann, J.L. (2010). Neuroimaging in Cockayne syndrome. AJNR Am. J. Neuroradiol. *31*, 1623–1630.

Lainé, J.P., and Egly, J.M. (2006). When transcription and repair meet: a complex system. Trends Genet. *22*, 430–436.

Maalouf, M., Rho, J.M., and Mattson, M.P. (2009). The neuroprotective properties of calorie restriction, the ketogenic diet, and ketone bodies. Brain Res. Brain Res. Rev. *59*, 293–315.

Mayne, L.V., and Lehmann, A.R. (1982). Failure of RNA synthesis to recover after UV irradiation: an early defect in cells from individuals with Cockayne's syndrome and xeroderma pigmentosum. Cancer Res. *42*, 1473–1478.

Menoni, H., Hoeijmakers, J.H., and Vermeulen, W. (2012). Nucleotide excision repair-initiating proteins bind to oxidative DNA lesions in vivo. J. Cell Biol. *199*, 1037–1046.

Mouchiroud, L., Houtkooper, R.H., Moullan, N., Katsyuba, E., Ryu, D., Cantó, C., Mottis, A., Jo, Y.S., Viswanathan, M., Schoonjans, K., et al. (2013). The NAD(+)/Sirtuin Pathway Modulates Longevity through Activation of Mitochondrial UPR and FOXO Signaling. Cell *154*, 430–441.

Pediconi, N., Guerrieri, F., Vossio, S., Bruno, T., Belloni, L., Schinzari, V., Scisciani, C., Fanciulli, M., and Levrero, M. (2009). hSirT1-dependent regulation of the PCAF-E2F1-p73 apoptotic pathway in response to DNA damage. Mol. Cell. Biol. *29*, 1989–1998.

Pleschke, J.M., Kleczkowska, H.E., Strohm, M., and Althaus, F.R. (2000). Poly(ADP-ribose) binds to specific domains in DNA damage checkpoint proteins. J. Biol. Chem. *275*, 40974–40980.

Puigserver, P., Wu, Z., Park, C.W., Graves, R., Wright, M., and Spiegelman, B.M. (1998). A cold-inducible coactivator of nuclear receptors linked to adaptive thermogenesis. Cell *92*, 829–839.

Robu, M., Shah, R.G., Petitclerc, N., Brind'Amour, J., Kandan-Kulangara, F., and Shah, G.M. (2013). Role of poly(ADP-ribose) polymerase-1 in the removal of UV-induced DNA lesions by nucleotide excision repair. Proc. Natl. Acad. Sci. USA *110*, 1658–1663.

Scheibye-Knudsen, M., Ramamoorthy, M., Sykora, P., Maynard, S., Lin, P.C., Minor, R.K., Wilson, D.M., 3rd, Cooper, M., Spencer, R., de Cabo, R., et al. (2012). Cockayne syndrome group B protein prevents the accumulation of damaged mitochondria by promoting mitochondrial autophagy. J. Exp. Med. *209*, 855–869.

Scheibye-Knudsen, M., Croteau, D.L., and Bohr, V.A. (2013a). Mitochondrial deficiency in Cockayne syndrome. Mech. Ageing Dev. *134*, 275–283.

Scheibye-Knudsen, M., Scheibye-Alsing, K., Canugovi, C., Croteau, D.L., and Bohr, V.A. (2013b). A novel diagnostic tool reveals mitochondrial pathology in human diseases and aging. Aging (Albany, N.Y. Online) *5*, 192–208.

Shimazu, T., Hirschey, M.D., Newman, J., He, W., Shirakawa, K., Le Moan, N., Grueter, C.A., Lim, H., Saunders, L.R., Stevens, R.D., et al. (2013). Suppression of oxidative stress by β-hydroxybutyrate, an endogenous histone deacetylase inhibitor. Science *339*, 211–214.

Sullivan, P.G., Rippy, N.A., Dorenbos, K., Concepcion, R.C., Agarwal, A.K., and Rho, J.M. (2004). The ketogenic diet increases mitochondrial uncoupling protein levels and activity. Ann. Neurol. *55*, 576–580.

Sutendra, G., Kinnaird, A., Dromparis, P., Paulin, R., Stenson, T.H., Haromy, A., Hashimoto, K., Zhang, N., Flaim, E., and Michelakis, E.D. (2014). A nuclear pyruvate dehydrogenase complex is important for the generation of acetyl-CoA and histone acetylation. Cell *158*, 84–97.

Tannahill, G.M., Curtis, A.M., Adamik, J., Palsson-McDermott, E.M., McGettrick, A.F., Goel, G., Frezza, C., Bernard, N.J., Kelly, B., Foley, N.H., et al. (2013). Succinate is an inflammatory signal that induces IL-1β through HIF-1α. Nature *496*, 238–242.

Thorslund, T., von Kobbe, C., Harrigan, J.A., Indig, F.E., Christiansen, M., Stevnsner, T., and Bohr, V.A. (2005). Cooperation of the Cockayne syndrome group B protein and poly(ADP-ribose) polymerase 1 in the response to oxidative stress. Mol. Cell. Biol. *25*, 7625–7636.

Weidenheim, K.M., Dickson, D.W., and Rapin, I. (2009). Neuropathology of Cockayne syndrome: Evidence for impaired development, premature aging, and neurodegeneration. Mech. Ageing Dev. *130*, 619–636.

Cell Metabolism, Volume *20*

Supplemental Information

A High-Fat Diet and NAD^+ Rescue Premature Aging in Cockayne Syndrome

Morten Scheibye-Knudsen, Sarah J. Mitchell, Evandro F. Fang, Teruaki Iyama, Theresa Ward, James Wang, Christopher A. Dunn, Nagendra Singh, Sebastian Veith, Md Mahdi Hasan-Olive, Aswin Mangerich, Mark A. Wilson, Mark P. Mattson, Linda H. Bergersen, Victoria C. Cogger, Alessandra Warren, David G. Le Couteur, Ruin Moaddel, David M. Wilson III, Deborah L. Croteau, Rafael de Cabo, and Vilhelm A. Bohr

Supplemental Information includes:

- **Extended experimental procedures**
- **Supplemental references**
- **Figure legends for figures S1-S6**
- **Table S1**
- **Supplementary figures S1-S6**

Extended experimental procedures

Animals. 4 month old mice were fed a standard AIN-93G diet (SD; carbohydrate:protein:fat ratio of 64:19:17 percent of kcal) *ad libitum* or at 40% CR, a SD supplemented with 100 mg/kg_{chow} resveratrol *ad libitum*, or a high fat diet *ad libitum* consisting of AIN-93G with 60% of calories from fat, primarily hydrogenated coconut oil (HFD; carbohydrate:protein:fat ratio of 16:23:61). Diets were purchased from Dyets Inc (DSM Nutritional Products North America, Parsippany, NJ). Resveratrol was provided by DSM Nutritional Products (Parsippany, NJ). WT and $Csb^{m/m}$ are on a C57Bl6 background. All measurements were done at 1 year of age. Unless otherwise stated, blood samples were collected after 6 hours of fasting at approximately 6 hours into the light cycle. Body weight and food intake were monitored every other week. Animal rooms were maintained at ~20°C and a 12-hour light/dark cycle. All animal protocols were approved by the Animal Care and Use Committee (352-LEG-2012) of the National Institute on Aging.

Metabolic assessment. Metabolic rate of the mice was assessed by indirect calorimetry in open-circuit oxymax chambers using the Comprehensive Lab Animal Monitoring System (CLAMS; Columbus Instruments, Columbus, OH, USA). Mice were single housed and maintained at ~24°C under a 12:12-h light-dark cycle (light period 0600–1800). Water and food were available *ad libitum* except for the CR mice. All mice were acclimatized to monitoring cages for 3-6 h after which twice-hourly, automated recordings of gas exchange were taken over the next 60 h. The concentrations of O_2 and CO_2 were monitored at the inlet and outlet of the sealed chambers to calculate respiration. The sensors were calibrated against a standard gas mix containing defined quantities of O_2, CO_2, and N_2. Constant airflow (0.6 L/min) was drawn through the chamber and monitored by a mass-sensitive flow meter. Each chamber was measured for 30 s at 30-min intervals. Movement (both horizontal and vertical) was monitored by beams 0.5 in apart on horizontal and vertical planes providing a high-resolution grid

covering the X, Y and Z planes. Beam breaks representing mouse movement were recorded in 30-s epochs. Body composition was measured before and after each trial. Food intake was monitored during the course of the experiment. The respiratory exchange ratio (RER) is simply the ratio between the carbon dioxide production and the oxygen consumption. For PJ34 injection experiments mice were acclimatized to monitoring cages for three days where daily saline injections were given. Body composition was measured using nuclear magnetic resonance spectroscopy before and after starting the experiment Food intake was monitored during the course of the experiment. The respiratory exchange ratio (RER) is simply the ratio between the carbon dioxide production and the oxygen consumption.

PJ34 and nicotinamide riboside *in vivo* experiment. 4 or 16 months old $Csb^{m/m}$ or WT male mice maintained on house chow (Harlan Teklad, Madison WI) for the course of the experiment. Five days prior to the experiment mice were handled and restrained daily to become accustomed to handling. At the commencement of the experiment, body composition was measured. Mice were placed into cages in the CLAMS system. Mouse cages were changed every three days. For the initial three days mice were given daily saline injections i.p. at 1100 hours and metabolism was measured as described above. On days 4-10 mice received PJ34 at a dose of 25 mg/kg i.p. (Tocris Bioscience, Bristol, UK) at 1100 hours and metabolism was measured as described above prior to the start of PJ34 treatment and immediately after body composition was measured. For nicotinamide treatments 4 month or 18 month old WT and $Csb^{m/m}$ mice were given daily injections of NR (500 mg/kg/d, ip) or saline for one week after which the mice were sacrificed and the cerebellum was removed for further experiments.

Body Composition. Measurements of lean body mass, fat and fluid mass in live mice were acquired by nuclear magnetic resonance (NMR) spectroscopy using the Minispec LF90 (Bruker Optics, Billerica, MA).

Oral Glucose Tolerance Test (OGTT). Following a three hour fast, mice received an oral gavage of 30% glucose solution (Sigma Aldrich, St Louis, MO) at a dose of 2g/kg body weight. Blood glucose was measured using an Ascensia Elite glucose meter at 0, 15, 30, 60 and 120 minutes following gavage.

Serum Chemistry. Glucose was measured in whole blood using the Ascensia Elite glucose meter (Bayer, Mishawaka, IN). Insulin was measured using an enzyme-linked immunosorbent assay (Crystal Chem, Downers Grove, IL) according to the manufacturer's instructions. Lactate was measured in serum using a Lactate Pro Test Meter according to the manufacturer's instructions (Kyoto, Japan).

Histology and EM. Animals were transcardially perfused via with PBS followed by 2.5% glutaraldehyde and 3% paraformaldehyde in PBS. Liver tissue for electron microscopy was transferred to 0.1M sodium cacodylate buffer (Electron Microscopy Sciences, Hatfield PA) for 24 hours at 4C. For transmission electron microscopy, samples were osmicated and embedded in Spurs resin. Ultra-thin (70-90nm) sections were taken from each block and twenty random fields were chosen from each liver and photographed for ultrastructural measurement using a Phillips CM10 Transmission Electron Microscope (magnification 1950x). Mitochondrial area was determined using image J (http://rsb.info.nih.gov/ij/). For scanning electron microscopy samples were osmicated, dehydrated, mounted and coated with platinum and liver sinusoidal endothelial porosity (percentage of the endothelial surface area occupied by fenestrations) was manually calculated on 10 sinusoids per liver using image J. The cerebellum was cut

into small specimens (typically 0.5 mm×0.5 mm×1 mm). The specimens were cryoprotected in glycerol and freeze substituted with Lowicryl HM20 according to an electron microscopic immunogold protocol (Bergersen et al., 2008). Ultrathin sections were cut (90 nm) using a diamond knife and dried at room temperature. The dried sections were counterstained with 1% uranyl acetate and 0.3% lead citrate. Electron micrographs were taken with a FEI Tecnai 12 electron microscope at primary magnifications of ×26500 and saved as tif files. Postsynaptic densities (PSDs) were identified in dendritic spines by their electron dense appearance, forming asymmetric synapses with nerve terminals. The length of the PSD was measured using ImageJ (http://imagej.nih.gov/ij/) and the "DistToPath" plugin (http://www.neuro.ki.se/broman/maxl/software.html). Histology of the liver and inner ear was performed by Histoserv (Histoserv, MD, USA) on the transcardially fixated tissue by staining with Masson's trichrome and hematoxylin and eosin respectively.

Microarray. Gene expression of WT and $Csb^{m/m}$ cerebellum was performed. Raw hybridization intensity data were log-transformed and normalized to yield z-scores. The z-ratio was calculated as the difference between the observed gene z-scores for the experimental and the control comparisons, and dividing by the standard deviation associated with the distribution of these differences. Z-ratio values =+2.0 or =-2.0 were chosen as cut-off values, defining increased and decreased expression, respectively. A complete set of 522 cellular pathways was obtained from the Molecular Signatures Database (MSigDB, Broad Institute, Massachusetts Institute of Technology, MA, USA). The complete set was tested for Geneset enrichment using Parametric analysis of Gene set enrichment (PAGE). For each pathway z-score, a p-value was computed using JMP 6.0 software to test for the significance of the z-score obtained. Principal component analysis was done using JMP 6.0. These tools were part of DIANE 1.0 (see http://www.grc.nia.nih.gov/branches/rrb/dna/diane_software.pdf for information).

Metabolomics. Metabolomic measurements were acquired by the West Coast Metabolomics Center. Briefly, mouse cerebellum tissue 20 mg FW was extracted using 1 mL of degassed acetonitrile:isopropanol:water (3:3:2; v/v/v) at -20°C, evaporated to dryness, and membrane lipids and triglycerides were removed in a clean-up using acetonitrile/water (1:1). Internal retention standards were added and samples were derivatized by 10 µL methoxyamine hydrochloride in pyridine (40 mg/ml) followed by 90 µl MSTFA (1 mL bottles, Sigma-Aldrich) for trimethylsilylation of acidic protons. Metabolomic analysis was conducted by injecting 0.5 µL of sample using a Gerstel MPS2 automatic liner exhange system (Mülheim, Germany) with cold injection system, separation on an Agilent 6890 gas chromatograph (Santa Clara, CA) equipped with a 30 m long, 0.25 mm i.d. Rtx5Sil-MS column, and mass spectra acquisition by a Leco Pegasus IV time of flight mass spectrometer (St. Joseph, MI) at a mass range of m/z 85–500 at 17 spectra s-1 and 1850V detector voltage, aquired with 280°C transfer line temperature, electron ionization at -70eV and an ion source temperature of 250°C. Result files were processed by BinBase database (http://fiehnlab.ucdavis.edu/projects/binbase_setupx), by matching retention index and mass spectra against the Fiehn mass spectral library of 1,200 compounds and the NIST05 commercial library. Final data were normalized to the average sum intensities for all known metabolites.

Open field. A mouse was placed in the center of a Plexiglas square measuring 23 inches X 23 inches. The open field was evenly illuminated and exploratory behavior was measured for 300 seconds using AnyMaze software (Wood Dale, IL). The apparatus was cleaned with 70% ethanol before testing the next mouse.

Treadmill. Mice were required to exercise on the treadmill until exhaustion. The treadmill was horizontal (0° incline) and mice ran in groups of 6. Subjects were habituated at a constant speed of 4 m/min for 5 minutes on day 1. The following day each mouse was given a trial starting at 7 m/min for 0-3 minutes, 12 m/min for 3-7 minutes, 15 m/min for 7-25 minutes, and 19 m/min for 25 minutes.

Hearing test. Mice were placed in a clear, plastic, rectangular box (23 inches x 23 inches) for a total of 300 seconds. Video and movement tracking were captured using ANY-Maze software (Stoelting Co. Wood Dale, IL). Two speakers, connected to a laptop, were placed at one end of the box on the same level as the top of the box. At 295 seconds, a previously recorded clap (108 db) was played on the speakers in order to test the capability of the mice to display a proper startle response when hearing a loud noise. Mice were subsequently scored for no response, possible response and definite response based on the video recording.

Cell culture. SV40-transformed CS1AN cells stably transfected with either CSB (WT CSB) or empty vector were cultured in DMEM supplemented with 10% FBS, 1% pen-strep, and 400 µg/ml geneticin and grown in 20% O2/5% CO2 at 37°C. PARP1 knockout HeLa cells were a kind gift of A. Mangerich, A. Bürkle, E. and Ferrando-May. Treatments done: resveratrol 100 µM for 48 hours; Srt1720 3 µM for 48 hours; NU1025 100 µM for 48 hours; PJ34 10 µM for 48 hours; 3AB 1 mM for 48 hours; β-OH-butyrate 10 mM for 48 hours; A-769662 10 µM for 48 hours; AICAR 1 mM for 48 hours; Dorsomorphin 5 µM for 48 hours; 3%O_2 treatment 72 hours; LW6 2.5/5 µM for 48 hours; siRNAs for 72 hours; 0.5 mM Oleic acid for 72 hours; 5 mM glucose for 72 hours; 100 µM EX-527 for 24 hours; 5/10/20 µM L002 for 24 hours; 50 µM MB-3 for 24 hours; 10 µM NU9056 for 24 hours; 5 µM C646 for 24 hours; 10 µM MG-132 for 5 hours.

Cellular oxygen consumption. Oxygen consumption and extracellular acidification rate measurements were performed using the Seahorse XF-24 instrument (Seahorse Biosciences, North Billerica, MA, USA). Cells were seeded into a Seahorse tissue culture plate. 24 h later media was changed to unbuffered XF assay media, pH 7.4 (Seahorse Biosciences, North Billerica, MA, USA) supplemented with 25 mM glucose (Sigma-Aldrich, St. Louis, MO, USA) and 1 mM sodium-pyruvate and 1 mM glutamax (Invitrogen, Carlsbad, CA, USA). Cells were incubated for 1 h at 37 °C at ambient O_2 and CO_2 levels. Respiration was measured in 4 blocks of 3 times 3 minutes. The first block measured the basal respiration rate. Next oligomycin (EMD chemicals, Gibbstown, NJ, USA) was added and the second block was measured. Then carbonyl cyanide 4-(trifluoromethoxy) phenylhydrazone (FCCP) (Sigma-Aldrich, St. Louis, MO, USA) was added and the third block was measured. Finally antimycin A (Sigma-Aldrich, St. Louis, MO, USA) was added and the last measurements were performed. Immediately after finishing the measurements cells were trypsinized and counted using a coulter counter (Beckman Coulter Inc., Brea, CA, USA). Lactate equilibrium was performed with XF-assay media supplemented with 25 mM glucose. First injection was 100 mM 2-deoxyglucose and subsequent injections were lactate (pH 7.4) as indicated.

Mitochondrial isolation and oxygen consumption. Tissues were homogenized in MAS-buffer (mannitol, sucrose, hepes) using a glass-teflon homogenizer and nuclei/debris was precipitated by a 1.000 g centrifugation for 10 minutes, 4°C. Supernatants were transferred to new tubes and mitochondria were precipitated by a 6.000 g centrifugation for 7 minutes, 4°C. The mitochondria were washed in MAS buffer and precipitated by a 6.000 g centrifugation for 7 minutes, 4°C. Mitochondria were resuspended in 500 µL MAS and 20 µL was injected into a pre-calibrated chamber in the Oroboros oxygraph (Oroboros, Innsbruck, Austria) containing 2 mL MAS supplemented with 5 mM succinate, 5 mM

pyruvate and 2 mM malate. State-4 respiration was measured and 3 mM ADP was injected and state-3 respiration was measured. The remaining mitochondrial suspension was flash frozen in liquid nitrogen and used for protein and citrate synthase measurements. For membrane potential and ROS production mitochondria were incubated for 15 minutes at 37°C in MAS supplemented with 5 mM succinate, 5 mM pyruvate and 2 mM malate, and 40 nM TMRM or 3 μM dihydroethidium.

NAD and ketone measurements. The NAD/NADH ratio was measured using a kit and following the provided protocol (Abcam, Cambridge, UK). For mass spectrometry 10^7 cells were suspended in 50 μl of deionized water, to which 250 μl of acetonitrile was added. The suspension was vortexed for 1 min, followed by centrifugation at 16,000 g at 4^{o}C for 5 min. The supernatant was collected and analyzed by mass spectrometry. The separations of the compounds were accomplished using a Zorbax XDB-C18 analytical column (50 x 4.6 mm i.d., 1.8 μm particles) purchased from Agilent (Palo Alto, CA, USA) following a previously described method with slight modification [reference below]. In brief, a linear gradient was run as follows: 0-5 min 10%B; 5-14 min 100%B; 14-15 min 100%B; 15-16 min 10%B; 16-20 min 10%B at a flow rate of 0.4 ml/min. The mobile phase consisted of water containing 0.05% trifluoroacetic acid (TFA) for component A and acetonitrile containing 0.02% TFA for component B. The total run time was 20 min per sample. Injection volume per sample was 50 μl. MS analysis was performed using an Agilent Technologies 1100 LC/MSD (Palo Alto, CA, USA) equipped with a G1322A degasser, G1312A binary pump, G1367A autosampler, G1316A column thermostat, G1315A diode array detector and G1946D mass spectrometer equipped with an electrospray ionization (ESI) interface. The analytes were monitored in the positive-ion mode for SIM at m/z 123.1 ($[M+H]^+$ of NAM), 335.1 ($[M+H]^+$ of NMN) and 664.1 ($[M+H]^+$ of NAD). Ketone bodies (β-hydroxybutarate) were measured in serum using a kit according to the manufacturer's instructions (Cayman Chemicals, Ann Arbor MI). ß-

hydroxybutyrate (BHB) levels in the brain tissue samples were measured using a previously described and validated LC/MS/MS method (Johansen and Windberg, 2011). In brief, brain tissue was spiked with 50 µL of 1 mM γ-hydroxybutyrate-d_6 (GHB-d_6). The sample was homogenized with 950 µL methanol. The sample was centrifuged at 14000 rpm for 15 min. The supernatant was analysed using a LC/MS/MS system. The chromatographic experiments were carried out on a Shimadzu Prominence high-performance liquid chromatography system (Shimadzu, Columbia, Maryland), and total analyte concentrations were determined using Zorbax SB C18 column (150 x 2.1 mm, Agilient technologies). An elution gradient, with mobile phases consisting of acidic water (0.1 % formic acid) and acidic methanol (0.1 % formic acid) (0–10 min: 0–10%; 11–16 min: 10–80%) respectively, separated the compounds within 20 min was utilized. The tandem mass spectrometry analysis was performed using a triple quadrupole mass spectrometer model API 4000 system from Applied Biosystems/MDS Sciex equipped with Turbo Ion Spray (Applied Biosystems, Foster City, California). Data were acquired and analyzed using Analyst version 1.4.2 (Applied Biosystems). Positive electrospray ionization data were acquired using multiple reaction monitoring, and quantification was accomplished using area ratios calculated using BHB-d_6 as the internal standard, where the concentration of the internal standard was set at 50 µM.

Acetyl-CoA measurements. Were performed using a kit and following the provided protocol (Sigma-Aldrich, St. Louis, MO, USA).

Acid extraction of histones. Histone were isolated as previously described (Shechter et al., 2007). Cells were preincubated at 2 mM glucose for 48 hours prior to treatments with 10 mM β-OH-butyrate or 10 µM PJ34.

Western, far-western and slot-blotting. Poly(ADP-ribose) was synthesized and purified as described previously (Popp et al., 2013). Purified recombinant proteins were either separated via denaturing polyacrylamide gel electrophoresis followed by semi-dry blotting or were directly immobilized on a nitrocellulose membrane using a slotblot manifold and vacuum. Subsequently, membranes with immobilized proteins were incubated with 0.2 µM poly(ADP-ribose) in TBST over night at 4°C, followed by high-stringency washes using 1M NaCl inTBST (3 times for 5 min at RT). Non-covalently bound poly(ADP-ribose) was detected using the anti-poly(ADP-ribose)-specific mAB 10H, anti-mouse HRP-coupled secondary antibody, and chemiluminescence detection.

Materials. Antibodies used in the study were purchased from the below companies: PAR (BD Pharmingen, #551813), PARP1 (Cell signaling, #9542), PARG1 (Abnova company, #H00008505-B01P), actin (abcam, #ab6276), Sirt1 (Santa Cruz, #sc-74465), Sirt2 (abcam, #ab51023), Sirt3 (Cell signaling, #5490), Sirt4 (Sigma, #S0948), Sirt5 (Sigma, #HPA022002), Sirt6 (Cell signaling, #12486), Sirt7 (Millipore, #ABE103), Bax (Cell signaling, #2772), Bcl-xL (Cell signaling, #2764), Bcl-2 (Cell signaling, #50E3), p65 (Cell signaling, #6956), ace-p65 (Cell signaling, #3045), p53 (Santa cruz,#SC-71818), ace-p53 (Cell signaling, #2570), UCP2 (Lifespan, #Ab-LS-B3249), Sir2.1 (Novus, #NB100-1923), PDK1 (Novus, #NB100-2383), PDK2 (abcam, #ab68164), PDK3 (Novus, #NBP1-54707), and PDK4 (abcam, #ab38242). A CSB antibody was raised in a rabbit against a peptide containing the c-terminal 1100-1300 amino acids of CSB and subsequent affinity purified against the antigen. siRNA against SIRT1, UCP2, p300, CBP, GCN5, PCAF, HIF-1α and HIF-2α were purchased from Origene.

Nematode studies. Bristol N2 (wild type) and csb-1 worms (ok2335) were purchased from the Caenorhabditis Genetics Centre (CGC) at the University of Minnesota, St. Paul, MN. csb-1 worms were outcrossed five times to the N2 prior to use. Lifespan analysis was performed at 25 °C for grown on classical NGM plates, or NGM plates supplemented with 25 mM β-hydroxybutyrate seeded with E. coli OP50 as food source (Fensgard et al., 2010). 25 L4 stage worms (Day 0) were transferred to 2 plates, to give synchronous populations of 50 animals per condition. Animals were scored as dead or alive and transferred every day to fresh plates seeded with E. coli OP50 during the fertile period, and then every day until death. Worms were considered dead when they stopped pharyngeal pumping and were unresponsive to touch. Worms that died because of internal bagging, desiccation due to crawling on the edge of the plates, or gonad extrusion were scored as censored. These animals were included in life-span analyses up to the point of censorship and were weighted by half in mortality calculations. We calculated mean, standard deviation of the mean, and P value using the log-rank test, from pooled population of animals. Figures display Kaplan Meier survival curves of pooled populations utilized for statistical analysis.

Microscopy. 5×10^4 cells were plated in 4 well chamber slides and grown overnight and fixed for 15 minutes in 3.7% paraformaldehyde in PBS. Cells were then washed before being permeabilized in 0.25% triton X-100 for 10 minutes on ice. Subsequently cells were washed in PBS and blocked over-night in PBS containing 5% FBS. Primary antibodies were added at a concentration of 1:100 and incubated for 1 hour at 37˚C. After being washed secondary antibodies were added at 1:1000 and incubated for 1 hour at 37˚C. Cells were then washed 6 times 10 minutes in PBS before being mounted in prolong antifade gold with DAPI (Invitrogen, Carlsbad, CA, USA). Images were acquired at 60 × magnification on a Nikon Eclipse

TE-2000e confocal microscope (Nikon, Tokyo, Japan). Quantification of foci was done using Volocity software (PerkinElmer, Waltham, MA, USA).

Flow cytometry. 2×10^5 cells were seeded in a 6 well culture dish. 24 hours later cells were washed in PBS once and trypsinized. Cells were then resuspended in DMEM without phenol red supplemented with 10% FBS containing 50 nM mitotracker Green FM (Invitrogen, Carlsbad, CA, USA), 20 nM TMRM (Invitrogen, Carlsbad, CA, USA) , 3 µM dihydroethidium (Invitrogen, Carlsbad, CA, USA) or 3 µM mitosox (Invitrogen, Carlsbad, CA, USA). Cells stained with TMRM were incubated for 15 minutes at 37°C while 30 minutes incubations were used for the rest of the stains. Fluorescence was measured by a flow cytometer (C6 Flow Cytometer, Accuri, Michigan, USA).

Biochemistry and recombinant proteins. PARP1 was purchased from Trevigen. Recombinant CSB was a gift from Dr. Tinna Stevsner. PARP1 activity was investigated by incubating 30 nM PARP1 with increasing doses of purified CSB in the presence of 10 nM double stranded DNA in the reaction buffer (1 mM NAD^+, 10 mM TRIS-HCl pH 8.0, 1 mM $MgCl_2$, 1 mM DTT) for 10 minutes at 37°C. The product was visualized by western blotting. UV-damaged DNA was generated by exposing a 39-mer double stranded DNA oligo to UV radiation for 10 minutes. Electro-mobility shift assay (EMSA) was performed by incubating PARP1 with DNA for 10 minutes at 37C after which increasing doses of CSB was added and further incubation was done for another 20 minutes at 37C. Reactions were performed in 20 mM HEPES-OH pH 8.0, 50 mM KCl, 200 µg/mL BSA, 5 mM DTT, and 5% (v/v) glycerol. Finished reactions were run on a 4% native polyacrylamide gel and visualized by Sybr Gold staining (Invitrogen, Carlsbad, CA, USA) on a ChemiDocTM MP (Bio-Rad, Hercules, CA, USA). BamH1 assay was performed by preincubating a 42-mer oligo containing a single BamH1 restriction site with 250 nM PARP1 for 20 minutes at 37C with or

without NAD^+. 125, 250 or 500 nM of CSB and 0.2 U BamH1-HF (New England Biolabs, Ipswich, MA,USA) was subsequently added and the reaction was further incubated 30 minutes at 37C. The reaction was performed in 20 mM HEPES-OH pH 8.0, 50 mM KCl, 4 mM $MgCl_2$, 200 µg/mL BSA, 5 mM DTT, and 5% (v/v) glycerol. The finished reaction was run on a 10% native gel and visualized by Sybr Gold staining (Invitrogen, Carlsbad, CA, USA) on a ChemiDocTM MP (Bio-Rad, Hercules, CA, USA).

Site-directed mutagenesis for substitutions K292A, K297A, K334A and K337A on CSB in CSB-GFP plasmid. Multiple substitutions for K292A, K297A, K334A and K337A on CSB in CSB-GFP plasmid was performed using QuikChange II Site-Directed Mutagenesis Kit (Agilent Technologies). The specific nucleotide changes corresponding to K292A and K297A on CSB in the plasmid was completed and then substitution for K334A and K337A was carried out. The two primer sets contain with the relevant nucleotide changes of K292A/K297A (forward primer; 5'-GTAATGCAAGAGCAGCTAGAGCAGCTCCAGCCCCAGTCACG-3', reverse primer; 5'-CTCGACGAGATCGACGAGAACGTAATGTTGGAACGAAGAA-3'), or K334A/K337A (forward primer; 5'-CCCTGGAACTGCAAAGCCCTCGCCTGGAGTGCCTTGATGTGCTTTTTCAAACG-3', reverse primer; 5'-CGTTTGAAAAAGCACATCAAGGCACTCCAGGCGAGGGCTTTGCAGTTCCAGGG-3'), respectively. PCR was carried according to the manufacturer's instruction. After digestion with DpnI (TaKaRa, Shiga, Japan), the DNA mix was transformed into NEB 5-alpha Competent E. coli (High Efficiency) (New England Biolabs) and then selected clones were sequence confirmed by Eurofins Genomics (Huntsville, AL, USA).

Protein Recruitment and Retention Experiments. To monitor protein recruitment and retention to laser induced DNA damage, localized microirradiation was performed as previously described in detail (McNeill et al., 2013). In brief, HeLa cells (2.0×10^5 cells) were precultured in a 35-mm glass bottom

culture dish with 10 mm diameter microwells (MatTek Corporation, Ashland, MA, USA) for 24 hr. GFP-tagged CSB (CSB-GFP) plasmid was transfected using JetPrime reagent (Polyplus-transfection, Illkirch, France) according to the manufacturer's standard protocol. The transfected cells were incubated for 24 hr before micropoint laser experiment. A 5 × 20 pixel (0.16 µm/pixel) region internal to the nuclei of the cells was targeted using a Plan Fluor ×60/1.25 numerical aperture oil objective. Throughout the experiment, the adhered cells were maintained at 80% humidity, 5% CO_2, and 37 °C using a live cell environmental chamber (Slonet Scientific, Segensworth, UK). To determine the effects of PARP inhibition on recruitment of CSB, 10 µM PJ-34 or 1 mM 3AB was added to the media one hour prior to laser microirradiation. The images were recorded using identical gain, exposure, sensitivity, and contrast settings, and analyzed with the Volocity software 6.2 (PerkinElmer, Waltham, MA, USA).

Statistics. Two-way ANOVA was used to determine significant difference across genotypes. Two-tailed t-tests were used to compare single groups using Graphpad prism (GraphPad Software, Inc., La Jolla, CA, USA).

Reference List

Bergersen,L.H., Storm-Mathisen,J., and Gundersen,V. (2008). Immunogold quantification of amino acids and proteins in complex subcellular compartments. Nat. Protoc. *3*, 144-152.

Johansen,S.S. and Windberg,C.N. (2011). Simultaneous determination of gamma-Hydroxybutyrate (GHB) and its analogues (GBL, 1.4-BD, GVL) in whole blood and urine by liquid chromatography coupled to tandem mass spectrometry. J. Anal. Toxicol. *35*, 8-14.

McNeill,D.R., Paramasivam,M., Baldwin,J., Huang,J., Vyjayanti,V.N., Seidman,M.M., and Wilson,D.M., III (2013). NEIL1 responds and binds to psoralen-induced DNA interstrand crosslinks. J. Biol. Chem. *288*, 12426-12436.

Popp,O., Veith,S., Fahrer,J., Bohr,V.A., Burkle,A., and Mangerich,A. (2013). Site-specific noncovalent interaction of the biopolymer poly(ADP-ribose) with the Werner syndrome protein regulates protein functions. ACS Chem. Biol. *8*, 179-188.

Shechter,D., Dormann,H.L., Allis,C.D., and Hake,S.B. (2007). Extraction, purification and analysis of histones. Nat. Protoc. *2*, 1445-1457.

Supplementary figure legends

Figure S1, related to figure 1. (A-C) daily food intake in the mice (n=12-14, mean ± SEM). (D-G) temperature levels in the mice (n=12-14, mean ± SEM). (H) and (I) Ambulatory movement of the mice in the metabolic cages as measured by double line breaks (n=12-14, mean ± SEM). (J) Representative images of transmission electron microscopy of the sinusoidal endothelium (e: endothelium, s: sinusoid, h: hepatocyte).

Figure S2, related to figure 2. (A) Venn diagrams of significantly changed genes when comparing HFD treatment to SD and HFD treatment to Resv. (B) Representative electron microscopy micrographs of the cerebellum of the mice (m: mitochondria, pf: Purkinje fibre, a: astrocyte, s: post-synaptic fibre, v: synapse). (C) Synaptic length (n=100-300, mean ± SEM). (D) Rotarod performance (n=11-14, mean ± SEM).

Figure S3, related to figure 2. (A) Distance travelled in open field test (n=11-14, mean ± SEM). (B) Speed travelled in the open field test (n=11-14, mean ± SEM). (C) Percent distance spend in the center in the open field test (n=11-14, mean ± SEM). (D) Distance travelled in a forced treadmill exercise (n=7-11, mean ± SEM). (E) Grip strength as measured by the time to fall from a wire of mice hanging by the for-limbs (n=11-14, mean ± SEM). (F) State-4 respiration of isolated mitochondria from the brain (n=5-8, mean ± SEM). (G) Respiratory control ratio (state-3 / state-4) (n=5-8, mean ± SEM). (H) State-3 respiration in isolated whole brain mitochondria after addition of 3 mM ADP using 2 mM malate, 4 mM succinate and 4 mM pyruvate as substrates (n=5-8, mean ± SEM). (I) State-4 respiration in isolated liver mitochondria (n=5-9, mean ± SEM). (J) State-3 respiration in isolated liver mitochondria after addition of 3 mM ADP using 2 mM malate, 4 mM succinate and 4 mM pyruvate as substrates (n=5-9, mean ± SEM). (K) The respiratory coupling ratio of liver mitochondria (n=5-9, mean ± SEM).

Figure S4, related to figure 2. (A) Lactate stimulated respiration of WT and CSB cells after inhibition of glycolysis and without other mitochondrial substrates in the assay medium (n=3 separate experiments, mean ± SEM). (B) Representative immunoblot of pyruvate dehydrogenase kinase isoforms in the cerebellum of WT and $Csb^{m/m}$ mice. Each lane is a separate mouse. (C) The lactate pyruvate equilibrium.

Figure S5, related to figure 5. (A) Alterations in the FCCP uncoupled respiration relative to basal respiration in WT and CSB cells (n=3-28 separate experiments, mean ± SEM). (B) Representative immunoblot of UCP2 protein levels in CSB and WT cells after transfection with a UCP2 encoding plasmid or knockdown using siRNA.

Figure S6, related to figure 4 and 6. (A) Flow cytometry of WT and CSB deficient cells treated with β-OHB and or EX-527 for 48 hours and stained with TMRM (n=6, mean ± SEM). (B) Representative immunoblot of SIRT1 and PAR levels after inhibition with PARP inhibitors. (C) Growth curves of WT and CSB deficient cells treated with increasing concentrations of L002 (n=3, mean ± SD). (D) Flow cytometry of WT and CSB deficient cells treated with MB-3, NU9056 or increasing concentration of L002 for 24 hours and stained with TMRM (n=3-12, mean ± SEM) (E) Growth curve of WT and CSB deficient cells treated with the histone acetyl transferase inhibitors MB-3 and NU9056. (F) Flow cytometry of WT and CSB deficient cells treated with C646 and stained with TMRM or mitosox (n=3, mean ± SEM). (G) Flow cytometry of WT and CSB deficient cells subjected to siRNA knockdown of various proteins and stained with TMRM (n=3, mean ± SEM). (H) Luciferase based SIRT1 promotor activity assay showing luminescence from WT and CSB deficient cells subjected to 24 hours L002 treatment (data normalized to ACTB promotor activity, n=3-6, mean ± SEM). (I) Representative far western of non-covalent CSB-PAR interaction.

GENE ONTOLOGY TERM	CSB saline vs WT (Z-score)	CSB saline vs WT (P-value)	CSB NR vs WT (Z-score)	CSB NR vs WT (P_value)
8137 NADH DEHYDROGENASE (UBIQUINONE) ACTIVITY	6.50	1.24E-15	1.10	0.24
4129 CYTOCHROME C OXIDASE ACTIVITY	5.44	2.52E-06	0.85	0.53
3954 NADH DEHYDROGENASE ACTIVITY	4.65	5.62E-14	0.67	0.34
5743 MITOCHONDRIAL INNER MEMBRANE	4.23	6.77E-04	-1.26	0.33
5739 MITOCHONDRION	3.98	2.30E-04	0.59	0.59
15986 ATP SYNTHESIS COUPLED PROTON TRANSPORT	3.28	1.51E-05	1.30	0.22
5746 MITOCHONDRIAL RESPIRATORY CHAIN	3.18	3.20E-03	0.14	0.90
46961 HYDROGEN ION TRANSPORTING ATPASE ACTIVIT	3.14	1.78E-04	1.82	0.07
16469 PROTON TRANSPORTING TWO SECTOR ATPASE CO	3.12	2.73E-05	1.79	0.08
46933 PROTON-TRANSPORTING ATP SYNTHASE ACTIVITY, ROTATIONAL MECHANISM	3.10	2.65E-04	1.71	0.09
302 RESPONSE TO REACTIVE OXYGEN SPECIES	2.74	1.49E-02	2.06	0.22
6122 MITOCHONDRIAL ELECTRON TRANSPORT, UBIQUINOL TO CYTOCHROME C	2.71	4.16E-03	0.62	0.64
45261 PROTON TRANSPORTING ATP SYNTHASE COMPLEX	2.67	1.10E-07	1.06	0.43
5751 MITOCHONDRIAL RESPIRATORY CHAIN COMPLEX	2.64	6.50E-03	0.44	0.52
45263 PROTON TRANSPORTING ATP SYNTHASE COMPLEX	2.57	1.59E-02	1.50	0.07
19825 OXYGEN BINDING	2.51	3.00E-03	0.39	0.80
6950 RESPONSE TO STRESS	2.50	4.60E-02	0.85	0.54
5747 MITOCHONDRIAL RESPIRATORY CHAIN COMPLEX	2.48	1.08E-03	0.64	0.56
6626 PROTEIN TARGETING TO MITOCHONDRION	2.32	2.04E-02	0.87	0.22
5753 MITOCHONDRIAL PROTON-TRANSPORTING ATP SYNTHASE COMPLEX	2.32	3.03E-03	-0.40	0.69
45454 CELL REDOX HOMEOSTASIS	2.00	4.29E-02	0.13	0.90
6120 MITOCHONDRIAL ELECTRON TRANSPORT, NADH TO UBIQUINONE	1.99	4.76E-03	0.68	0.35
42542 RESPONSE TO HYDROGEN PEROXIDE	1.83	3.27E-02	0.52	0.53
16651 OXIDOREDUCTASE ACTIVITY ACTING ON NADH	1.80	4.54E-03	0.51	0.60
7568 AGING	1.52	3.03E-02	1.42	0.39
16575 HISTONE DEACETYLATION	-1.50	2.28E-02	-0.53	0.50
10212 RESPONSE TO IONIZING RADIATION	-1.54	7.97E-03	-1.50	0.03
51091 POSITIVE REGULATION OF SEQUENCE-SPECIFIC DNA BINDING TRANSCRIPTION FACTOR ACTIVITY	-1.68	3.19E-02	0.26	0.67
42393 HISTONE BINDING	-1.73	1.10E-02	1.09	0.36
12 SINGLE STRAND BREAK REPAIR	-1.83	6.86E-03	-0.09	0.94
120 RNA POLYMERASE I TRANSCRIPTION FACTOR COMPLEX	-1.88	4.48E-05	-0.53	0.49
51090 REGULATION OF SEQUENCE-SPECIFIC DNA BINDING TRANSCRIPTION FACTOR ACTIVITY	-1.93	2.32E-02	-0.39	0.69
3684 DAMAGED DNA BINDING	-2.14	3.20E-02	0.14	0.87
16564 TRANSCRIPTION REPRESSOR ACTIVITY	-2.21	1.62E-02	-1.25	0.28
122 NEGATIVE REGULATION OF TRANSCRIPTION FROM RNA POLYMERASE II PROMOTER	-2.47	3.97E-03	0.54	0.58
123 HISTONE ACETYLTRANSFERASE COMPLEX	-2.47	5.00E-02	-0.12	0.89
4386 HELICASE ACTIVITY	-2.52	4.43E-04	-0.72	0.43
16874 LIGASE ACTIVITY	-2.67	2.96E-03	-1.52	0.09
4402 HISTONE ACETYLTRANSFERASE ACTIVITY	-2.78	1.41E-03	-0.32	0.66
6310 DNA RECOMBINATION	-2.87	3.88E-03	-1.29	0.08
6974 RESPONSE TO DNA DAMAGE STIMULUS	-3.19	1.60E-03	0.22	0.82
16571 HISTONE METHYLATION	-3.38	2.90E-04	-1.31	0.23
16573 HISTONE ACETYLATION	-3.54	9.99E-04	-0.50	0.53
6281 DNA REPAIR	-4.16	1.09E-05	-0.68	0.49
6355 REGULATION OF TRANSCRIPTION, DNA-TEMPLATED	-5.46	3.27E-07	-1.76	0.09
6350 TRANSCRIPTION	-5.77	9.27E-09	-1.62	0.11

Table S1, related to figure 7. A list of Gene Ontology Terms that are significantly changed when comparing old $Csb^{m/m}$ saline treated mice vs old WT saline treated and old $Csb^{m/m}$ nicotinamide riboside treated mice vs old WT saline mice.

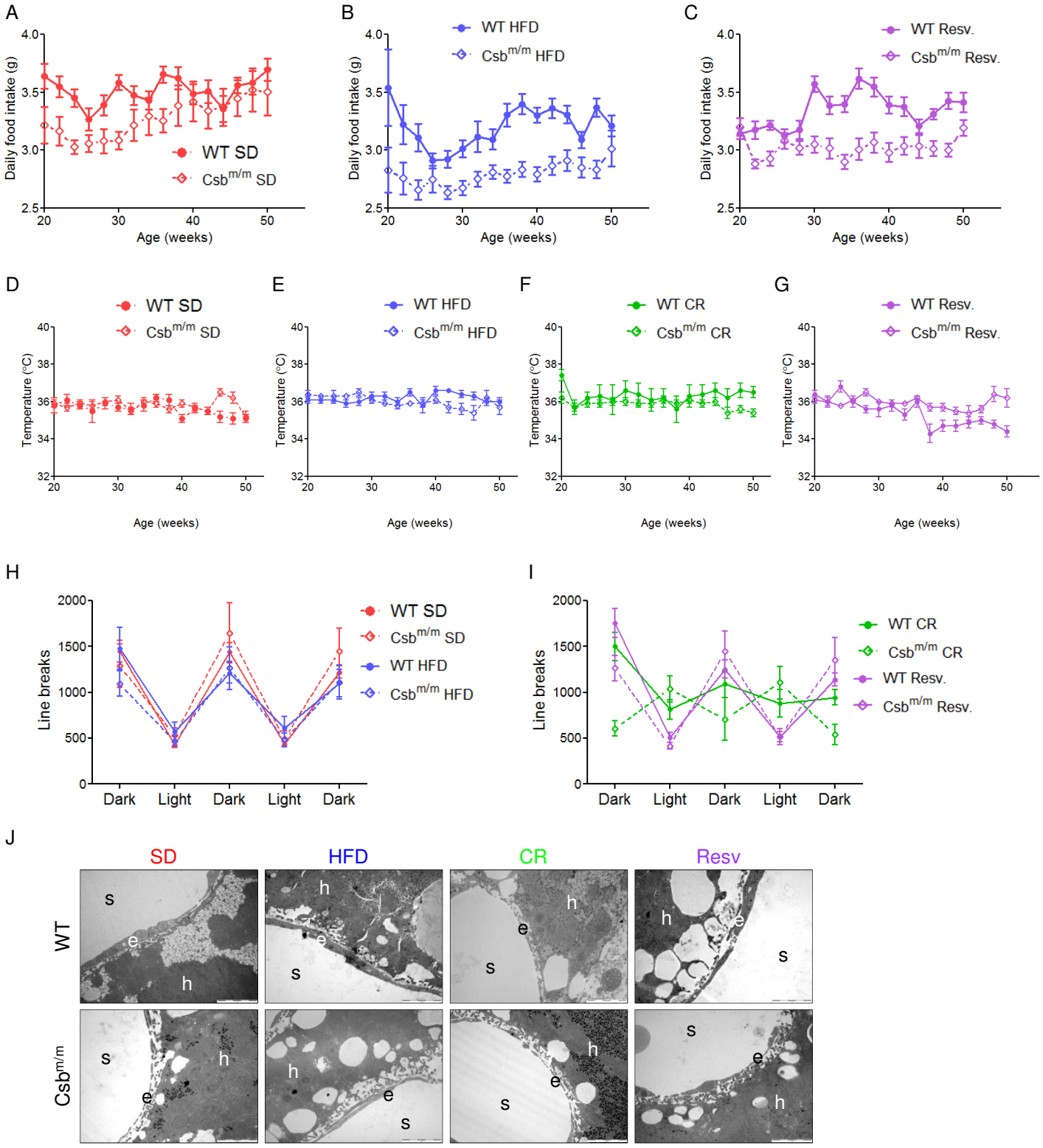
A
Daily food intake (g)
Age (weeks)
WT SD
Csb^m/m SD
B
WT HFD
Csb^m/m HFD
C
WT Resv.
Csb^m/m Resv.
D
Temperature (°C)
E
F
WT CR
Csb^m/m CR
G
H
Line breaks
Dark
Light
I
J
SD
HFD
CR
Resv
WT
Csb^m/m
s
e
h

Figure S1

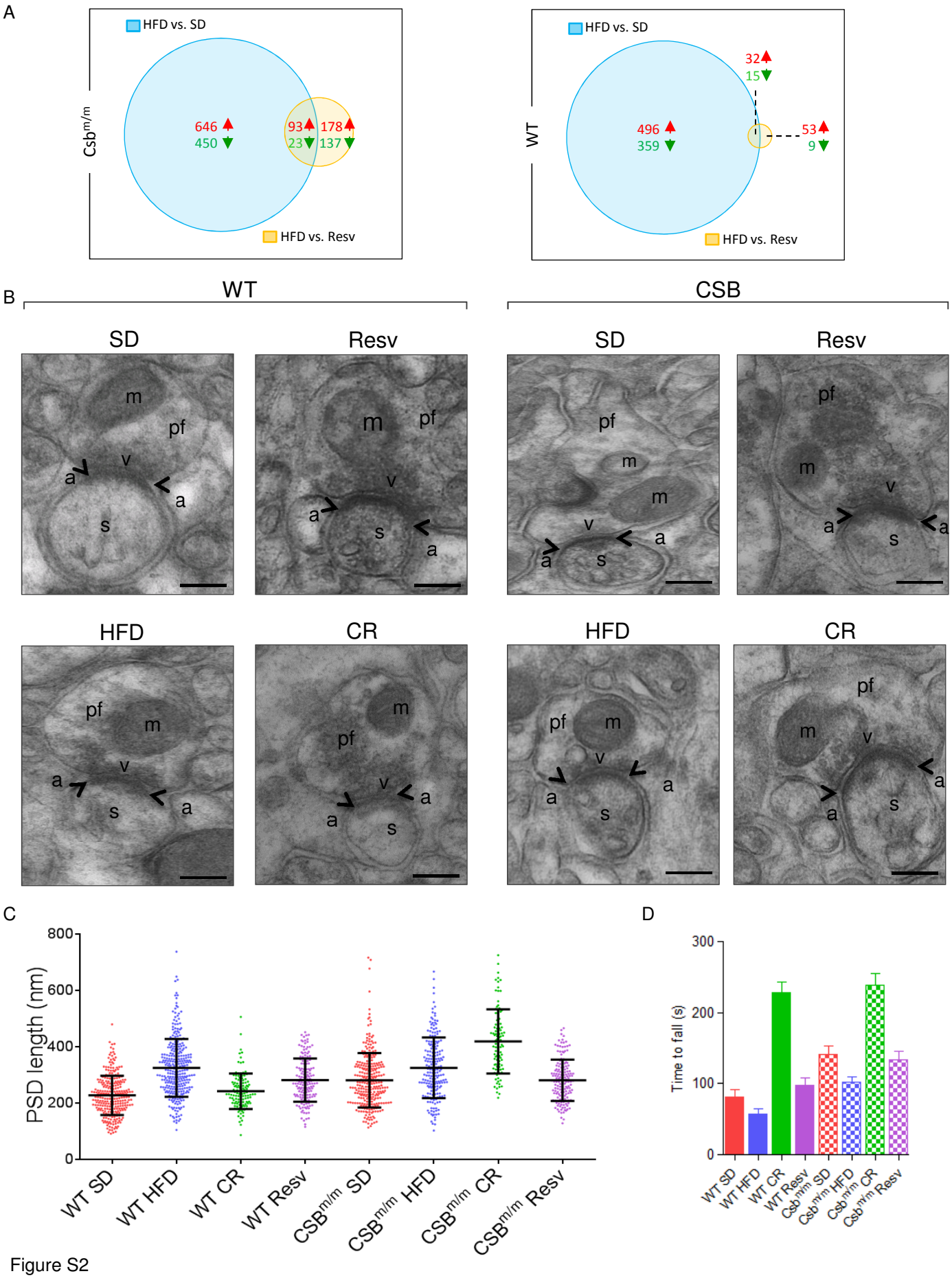
A
HFD vs. SD
Csb m/m
646
450
93
23
178
137
HFD vs. Resv
HFD vs. SD
WT
32
15
496
359
53
9
HFD vs. Resv
B
WT
CSB
SD
Resv
SD
Resv
HFD
CR
HFD
CR
m
pf
v
a
s
C
PSD length (nm)
800
600
400
200
0
WT SD
WT HFD
WT CR
WT Resv
CSB m/m SD
CSB m/m HFD
CSB m/m CR
CSB m/m Resv
D
Time to fall (s)
300
200
100
0
WT SD
WT HFD
WT CR
WT Resv
Csb m/m SD
Csb m/m HFD
Csb m/m CR
Csb m/m Resv

Figure S2

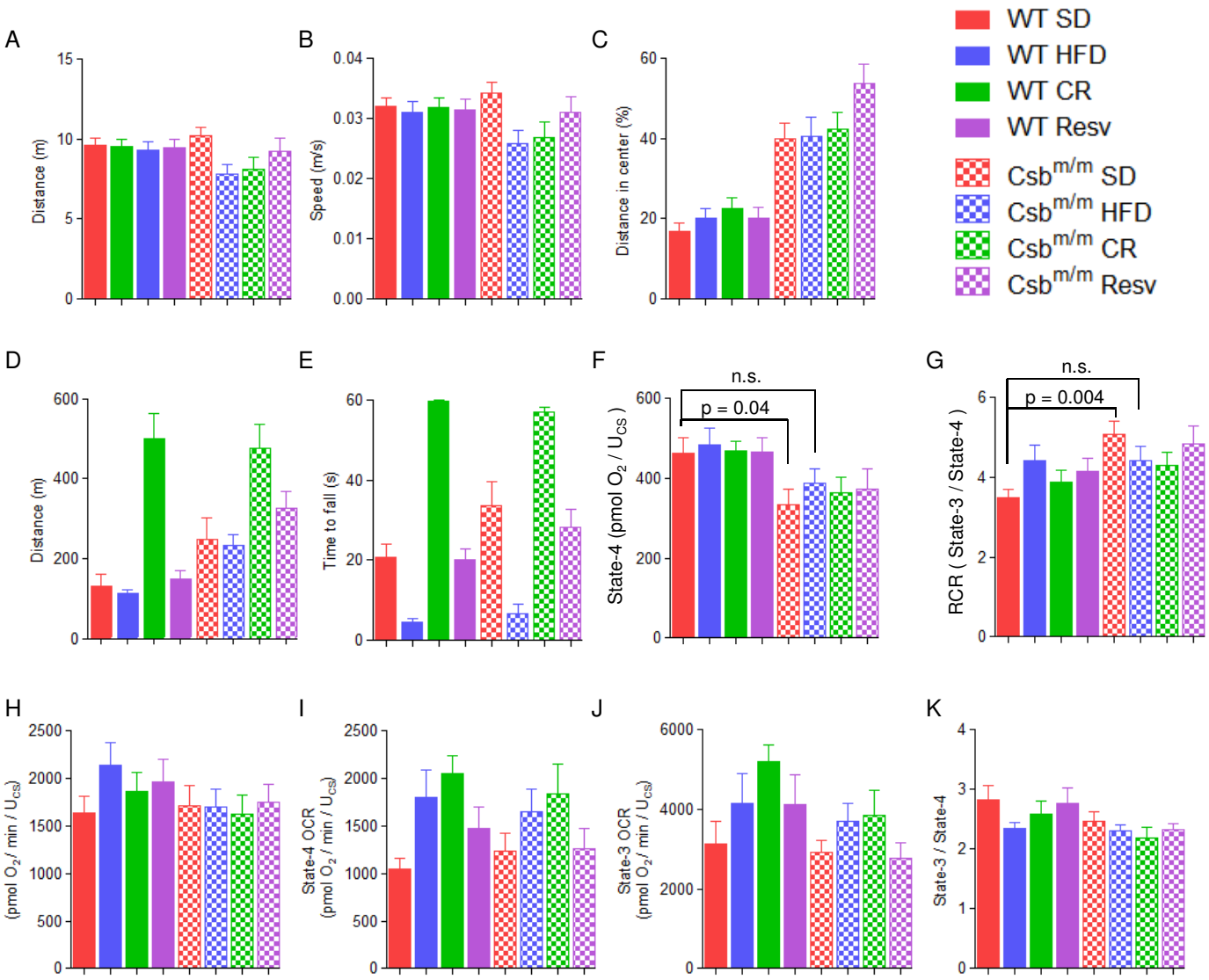
A
B
C
D
E
F
G
H
I
J
K
WT SD
WT HFD
WT CR
WT Resv
Csb m/m SD
Csb m/m HFD
Csb m/m CR
Csb m/m Resv
Distance (m)
Speed (m/s)
Distance in center (%)
Distance (m)
Time to fall (s)
State-4 (pmol O2 / UCS)
n.s.
p = 0.04
RCR (State-3 / State-4)
n.s.
p = 0.004
State-3 OCR (pmol O2 / min / UCS)
State-4 OCR (pmol O2 / min / UCS)
State-3 OCR (pmol O2 / min / UCS)
State-3 / State-4

Figure S3

A

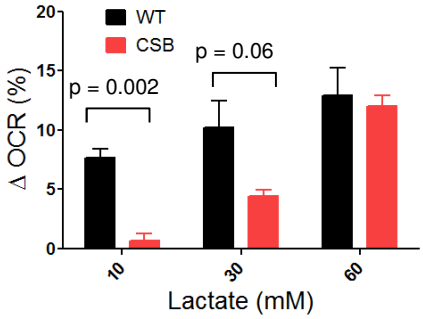

B

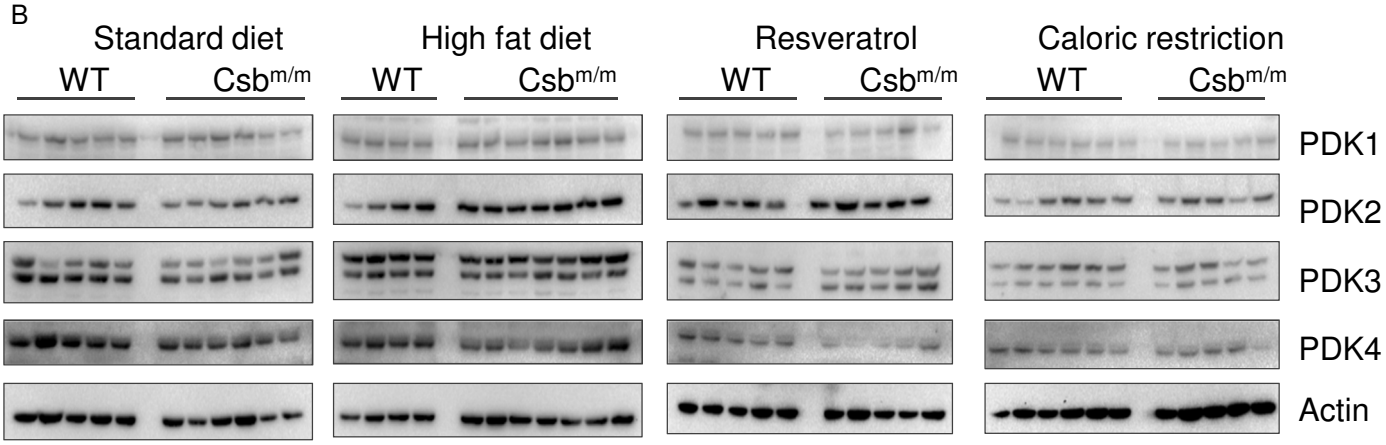

C

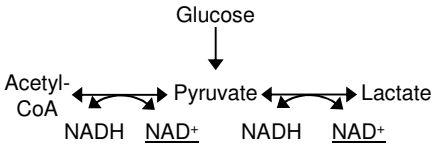

Figure S4

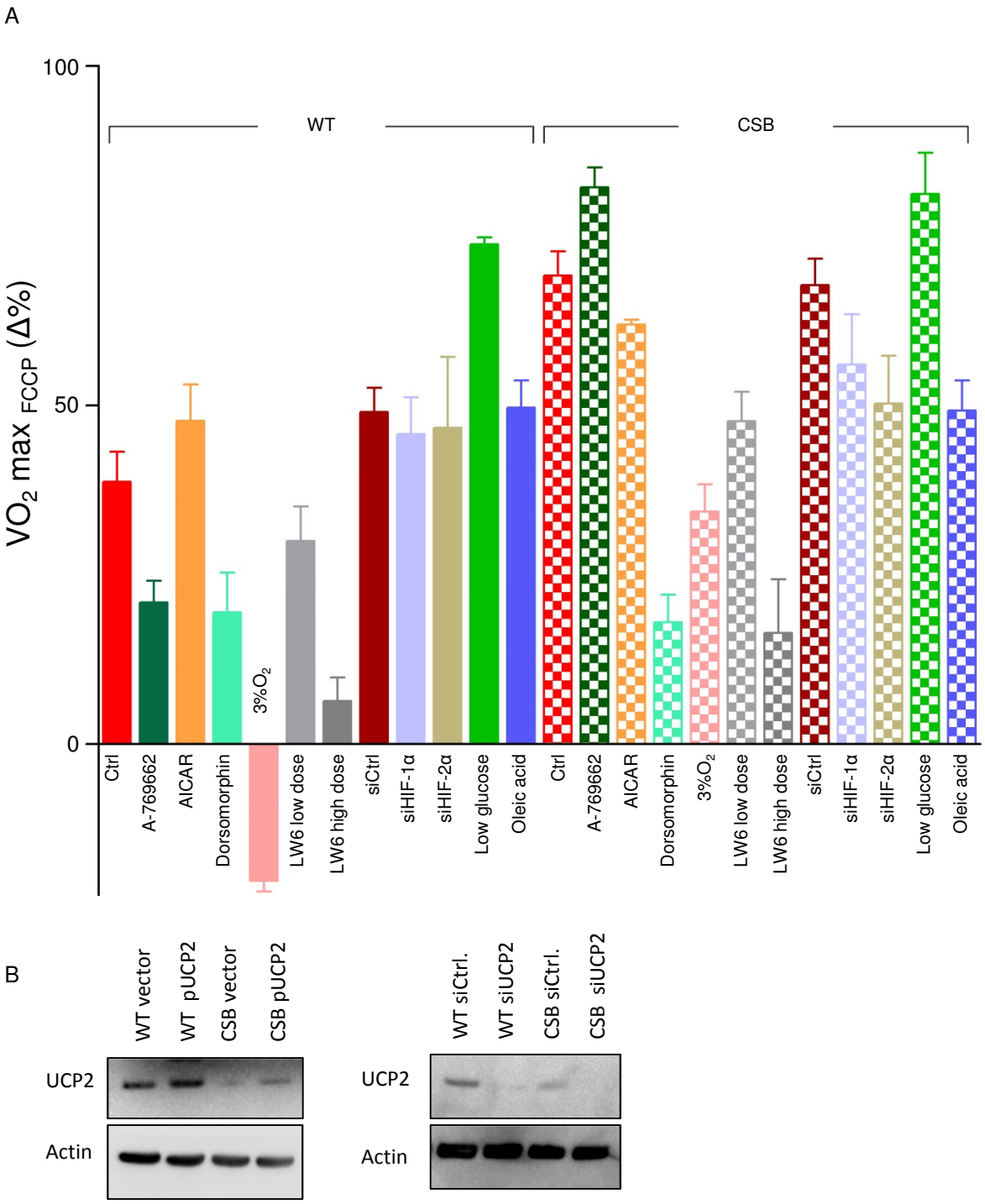
A
100
50
0
VO_2 max $_{FCCP}$ (Δ%)
WT
CSB
Ctrl
A-769662
AICAR
Dorsomorphin
3%O_2
LW6 low dose
LW6 high dose
siCtrl
siHIF-1α
siHIF-2α
Low glucose
Oleic acid
Ctrl
A-769662
AICAR
Dorsomorphin
3%O_2
LW6 low dose
LW6 high dose
siCtrl
siHIF-1α
siHIF-2α
Low glucose
Oleic acid
B
WT vector
WT pUCP2
CSB vector
CSB pUCP2
UCP2
Actin
WT siCtrl.
WT siUCP2
CSB siCtrl.
CSB siUCP2
UCP2
Actin

Figure S5

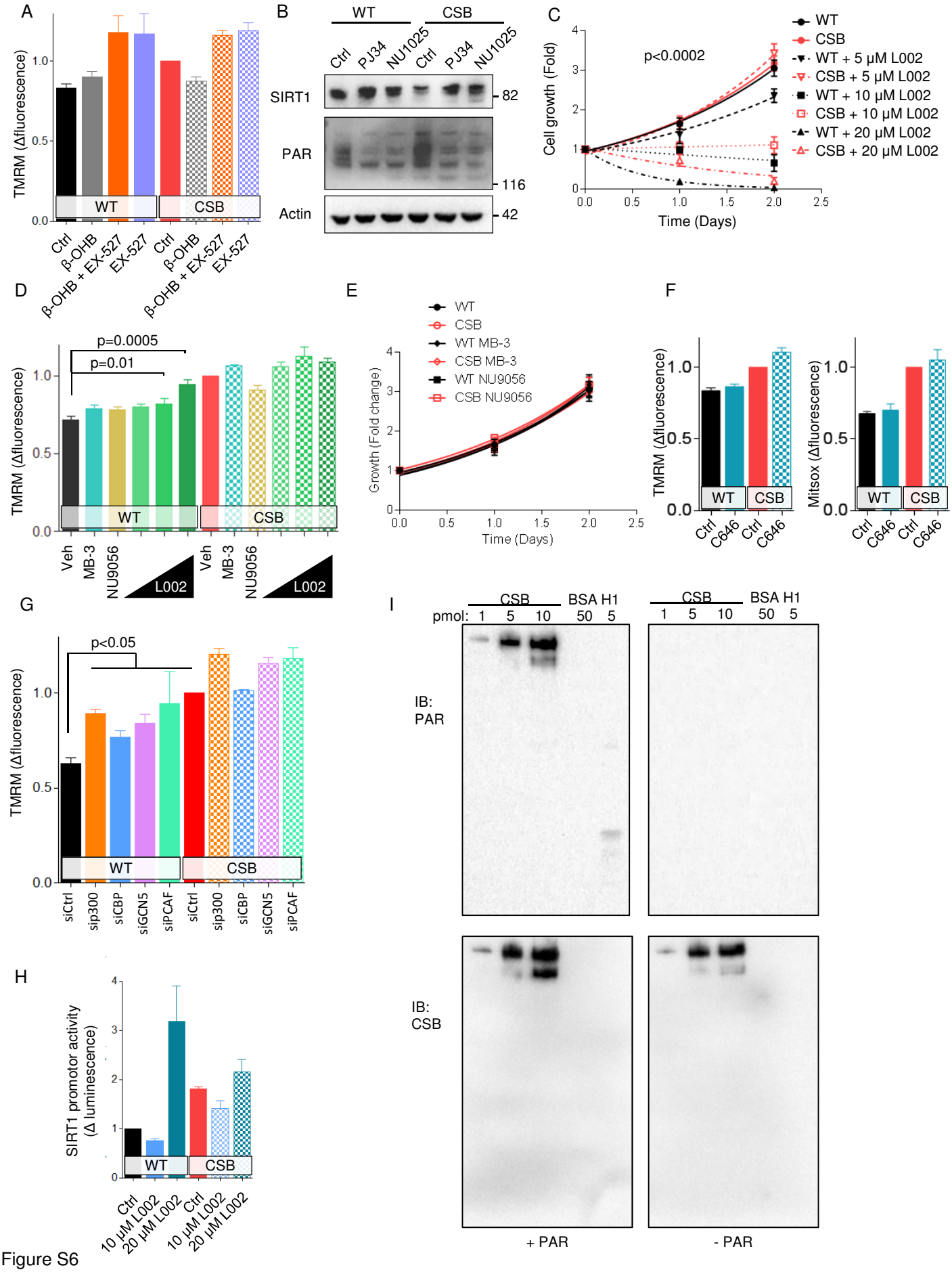
A
TMRM (Δfluorescence)
WT
CSB
Ctrl
β-OHB
β-OHB + EX-527
EX-527
B
WT
CSB
Ctrl
PJ34
NU1025
SIRT1
PAR
Actin
82
116
42
C
Cell growth (Fold)
p<0.0002
Time (Days)
WT
CSB
WT + 5 μM L002
CSB + 5 μM L002
WT + 10 μM L002
CSB + 10 μM L002
WT + 20 μM L002
CSB + 20 μM L002
D
TMRM (Δfluorescence)
p=0.0005
p=0.01
Veh
MB-3
NU9056
L002
E
Growth (Fold change)
Time (Days)
WT
CSB
WT MB-3
CSB MB-3
WT NU9056
CSB NU9056
F
TMRM (Δfluorescence)
Mitsox (Δfluorescence)
Ctrl
C646
G
TMRM (Δfluorescence)
p<0.05
siCtrl
sip300
siCBP
siGCN5
siPCAF
H
SIRT1 promotor activity
(Δ luminescence)
Ctrl
10 μM L002
20 μM L002
I
CSB
BSA H1
pmol: 1 5 10 50 5
IB:
PAR
IB:
CSB
+ PAR
- PAR

Figure S6